2013-05-10

An Exploration of Carbon-Filled Carbon Nanotubes as a Potential Material in Coronary Stents

Kristopher Neil Jones
Brigham Young University - Provo

An Exploration of Carbon-Filled Carbon Nanotubes as a Potential Material in Coronary Stents

Kristopher N. Jones

A thesis submitted to the faculty of
Brigham Young University
in partial fulfillment of the requirements for the degree of

Master of Science

Brian D. Jensen, Chair
Larry L. Howell
Anton E. Bowden

Department of Mechanical Engineering

Brigham Young University

April 2013

ABSTRACT

An Exploration of Carbon-Filled Carbon Nanotubes as a
Potential Material in Coronary Stents

Kristopher N. Jones
Department of Mechanical Engineering, BYU
Master of Science

The purpose of this research is to explore the potential of using carbon-infiltrated carbon nanotubes (CI-CNT) as a material for coronary artery stents. Stents are commonly fabricated from metal, which may not perform as well as many polymers and ceramics in biomedical applications. Pyrolytic carbon, a ceramic, is currently used in medical implant devices due to its preferrable biocompatibility properties. Micro-patterned pyrolitic carbon devices can be created by growing carbon nanotubes, and then filling the space between with amorphous carbon via chemical vapor deposition.

We prepared multiple samples of two different planar stent-like flexible geometries and smaller cubic structures out of carbon infiltrated carbon nanotubes. These samples were tested in tension to failure. The cubic structures were used for separate compression tests. We also examined existing auxetic patterns for possible application in the stent designs and a second iteration of design and fabrication was performed using data and understanding obtained from the work in the first iteration. Slight changes were made to the mask design and fabrication processes based on the new geometries and testing considerations. The auxetic planar designs were tested in compression to demonstrate flexibility and collect material data.

The testing results show that CI-CNTs can be designed and fabricated into flexible geometries capable of stent-like compression. The samples in this work were found to have moduli ranging from 5 to 27 GPa, with the majority being between 10 and 20 GPa. We also found fracture strength greater than 100 MPa, with it sometimes getting as high as 200 MPa. Lastly, fracture strain values were measured, with the maximum reaching 1.4% and the average between 0.75-1%. We also found that the CI-CNTs material lends itself to fracture at weak locations (if present) before the anticipated fracture strength has been reached and concluded that a tightly controlled process (including fabrication machines) environment is necessary to ensure consistent results and a CI-CNT material whose imperfections have been minimized.

Keywords: coronary stent, carbon nanotubes, CNT, microfabrication, compliant mechanism, pyrolytic carbon

ACKNOWLEDGMENTS

It would be wrong for me to not take this opportunity to acknowledge all the individuals and institutions that have assisted and provided guidance and/or support to me throughout this work.

I am grateful to Brigham Young University and specifically, the Ira A. Fulton College of Engineering and Technology and the College of Physical and Mathematical Sciences for the use of their facilities and resources. I acknowledge Clarke Capital Partners for their support and funding in part of this work.

I would like to express my appreciation to the members of my graduate committee including: Dr. Brian D. Jensen (Graduate Advisor), Dr. Larry L. Howell, and Dr. Anton Bowden. Additionally, I must mention Dr. Robert Davis and Dr. Richard Van Fleet of the Physics Department. Each of these professors provided support and insight which helped my research progress. I wish to specifically thank Dr. Jensen for accepting me as his graduate student and being a source of stability throughout the research process.

I was fortunate to be part of the Compliant Mechanism Research Laboratory. I am grateful for and acknowledge the help of other graduate and undergraduate students. I enjoyed collaborating with them regarding challenges both in research and coursework. I wish to specifically mention the efforts of Jason Lund. He is a student of many talents including competence in microfabrication processes, ANSYS modeling, MATLAB programming, and general problem solving, and was ever willing to assist me when a challenge arose.

My parents and siblings have been a source of support and examples of exellence since I began my education. I thank my parents for teaching me the importance of learning and working. I thank my siblings for their encouragement and motivation regarding my educational pursuits.

Lastly, this effort would have been impossible without the unwaivering support of my lovely wife Brittney and the love of our sweet daughters Macey and Lily. They have sacrificed many hours of my absence while I worked toward my educational goals.

TABLE OF CONTENTS

LIST OF TABLES

LIST OF FIGURES

CHAPTER 1. INTRODUCTION

1.1 Background

Modern medical advances in equipment, materials and procedures are continually reducing the number of preventable deaths, especially in industrialized countries like the United States [1]. Even with these advances, however, physicians, surgeons, and biomedical engineers still have much work ahead of them to improve treatments and mortalitity rates further. According to the Center for Disease Control, the leading cause of death in the United States is Heart Disease, claiming approximately 23.7% of all deaths, usurping cancer at 22.8% percent [2, 3]. Heart Disease is a broad term which encapsulates multiple illnesses and challenges associated with the cardiovascular system [4]. Among these, coronary artery disease accounts for half of all Heart Disease deaths, or approximately 11.85% of all deaths in the United States. Coronary artery disease, also called coronary heart disease, is a condition where blood vessels which supply blood and oxygen to the heart narrow, thus reducing the critical flow rate of blood [3, 5]. This reduced blood flow causes the heart to strain, which is felt by pain in the chest, shortness of breath, fatigue, and in the worst cases, heart failure. The vessel itself is narrowed not by the artery growing smaller, but by fatty plaque build up on the inner walls [3]. Figure 1.1 depicts a typical scenario of plaque build up in the coronary artery.

To combat and treat cornary artery disease, physicians and surgeons first attempt non-invasive methods. If these methods are unsuccessful in treating the problem, percutaneous procedures are used further to address the plaque build up. Balloon angioplasty is a procedure where a surgeon inserts a small, unpressurized balloon into the patient, typically through the femoral artery, and directs it to the plaque-affected artery. Once in place, the balloon is carefully pressurized and expands the narrowed section of artery. The balloon is then unpressurized and removed from the patient, having expanded the affected area [7]. Balloon angioplasty, however, can be considered a temporary solution as the artery wall can, after being expanded, constrict back to typical size, and

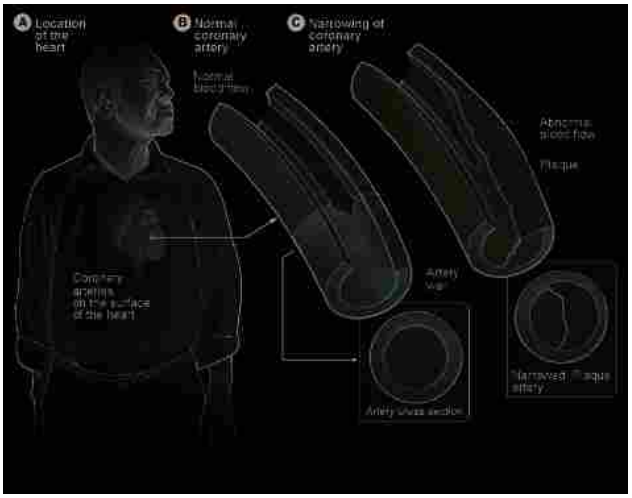

Figure 1.1: Image representation of typical plaque build up in coronary artery from [6]

since the plaque is still present, the vessel once again becomes narrowed. Additional angioplasty procedures could be performed, or a more permanent procedure using a stent could be performed.

A stent is a flexible, tubular mesh which physicians surgically insert into the passages of the human body for purposes including the reduction of localized flow constriction and supporting a collapsed passageway. Like balloon angioplasty, a stent is percutaneously inserted into the affected area with an unpressurized balloon. The balloon is pressurized which both expands the artery and plastically deforms the stent to a larger diameter. The balloon is removed while the stent remains in the artery as a "scaffold" system to prevent the artery from reocclusion. Figure 1.2 shows a typical cornary stent implantation example. Bare metal stents (BMS) were initially made from stainless steel, a material known to resist corrosion and also capable of tolerating high stress, even plastic deformation, without fracture. For many engineering applications, stainless steel is an appropriate choice because of its strength, well-understood and repeatable properties, and reasonable cost. However, it may not react as well as other materials, namely ceramics and polymers, with the body in biomedical applications [8]. Much of the work addressing this issue concerns the coating of the steel in drug eluting polymers to improve biocompatibility, creating a drug eluting stent (DES), rather than an investigation on stent material itself.

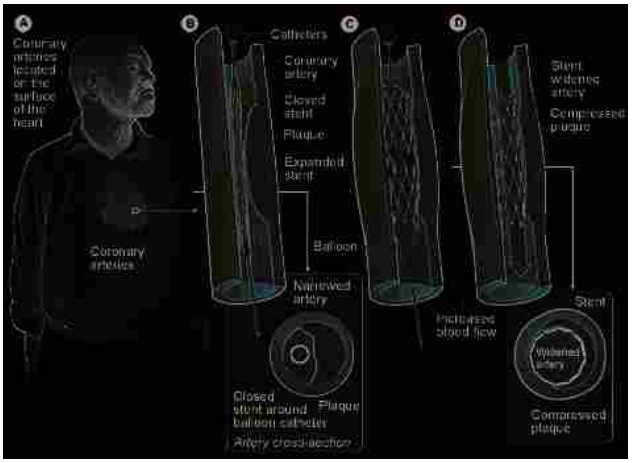

Figure 1.2: Image depicting a typical stent application in blood vessel from [9]

1.1.1 Stent Challenges

There are two main challenges hindering the success of stent implantation: restenosis and thrombosis. Restenosis is the recurrence of stenosis, which is the narrowing of a blood vessel leading to restricted blood flow. In stent implantation, restenosis is seen as tissue growing from the artery wall onto and over the stent as an immune system response to protect the body [3]. To the body, stents are foreign objects and materials which are therefore acted upon by the body's various methods of defense, causing these well known stent problems. Over time, this restenosis tissue becomes scar tissue and begins to hinder blood flow, increasing the risk of dangerous blood clots within the vessel [10]. The other common problem is thrombosis, defined as the formation of a blood clot which further restricts blood flow. Reduced blood flow from restenosis or thrombosis can lead to a myriad of health problems. Thrombotic events remain the primary cause of death after percutaneous coronary interventions are performed [11].

Studies on both BMSs and DESs have sought to quantify likelihood of restenosis and thrombosis. For example, one experiment included 238 patients at 19 medical centers where a BMS stent was implanted. Of these, 26.6% of patients experienced at least 50% restenosis at one year and 23% of the patients underwent further percutaneous revascularization [12]. Another trial compared the results of a DES and BMS with identical geometry in 1058 patients. After eight months in the BMS trial, 35.5% encountered at least 50% restenosis, 0.8% encountered stent thrombosis, and 16.6% required revascularization while in the DES trial, 3.2% encountered the

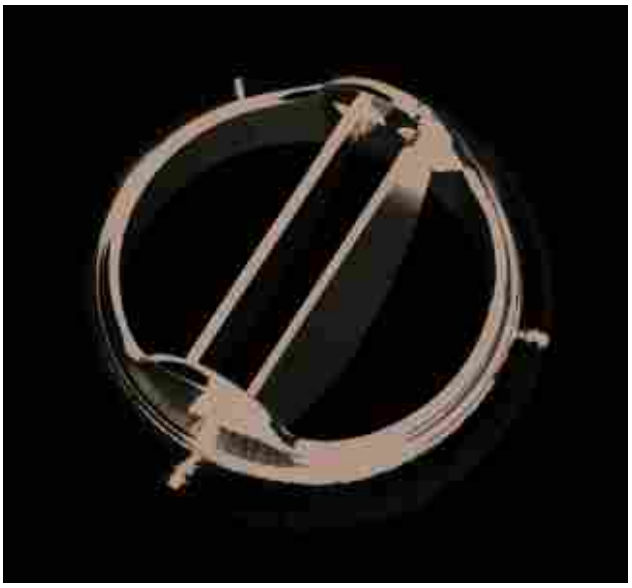

Figure 1.3: Example of pyrolytic carbon already successfully used in medical application from [14]

same restenosis, 0.4% encountered stent thrombosis, and 4.1% required revascularization [13]. While these results show much improvement of the DES over a BMS and are reflected in other samplings, improvements to even the DES could potentially still be made by addressing the stent material itself. After the coating of a DES completely wears off, essentially a BMS is left with higher likelihood of restenosis, thrombosis, and revascularization. Materials have been discovered or engineered to be more biocompatible than others. Many of these materials fall in the category of ceramics. A biocompatible ceramic stent could reduce this likelihood even lower than that of DES.

1.1.2 Application of Pyrolytic Carbon

There is much research in the area of biocompatible materials and more specifically, carbon materials. Carbon and carbonaceous materials are generally well tolerated by animal cells and are therefore commonly used in various types of medical implants [15–17]. Carbon has been used in such applications as finger bone replacement implants and heart valve replacements [18]. More specifically, while the biocompatibility of pyrolytic carbon with blood and tissue is not perfect, it has performed well enough to be used in over 500,000 heart valve components [16]. Figure 1.3 shows one example of pyrolytic carbon used in a medical application. Further investigation into

the biocompatibility of pyrolytic carbon shows that not only the chemical composition, but also the surface of the material itself play an important role in the body's reaction to this foreign material [15]. It is not uncommon to design an implant constructed from steel or titanium because of their superior mechanical behavior, but coat the implant in pyrolytic carbon to keep the body from adversely reacting to the bare metal. This is the case with metal stents being coated with pyrolytic carbon [17]. The carbon-infiltrated carbon nanotube (CI-CNT) material produced in this research is a pyrolytic carbon which can be made into designs similar to coronary arterial stents.

1.1.3 CI-CNT MEMS Fabrication

A review of the literature shows that investigation into CI-CNT MEMS and MEMS-like fabrication is extensively researched. The process used in this research comes not only from CNT growth and infiltration methods, but also from methods to pattern or shape the CI-CNT material. For example, Hutchison et al. discuss the use of CNTs as a framework in producing high aspect ratio MEMS and demonstrate how to control the growth of VACNTs (vertically aligned carbon nanotubes) [19]. Moulton investigates a portion of the process specifically related to the straightness and height of CNTs [20]. Rather than a typical, "spaghetti"-like, random growth, CNTs are grown vertically and can therefore produce complicated structural geometry, better reflecting the intended design [19]. While this paper shows this application with a silicon filled CNT structure, the same methods can be implemented with a carbon filled CNT structure. In each case, the properties of the structure are determined not by the CNTs, but by the filled material.

Typical ceramics have undesirable properties when considering their use in compliant designs. They are known for their high strength and temperature resistance capabilities, but easily fracture and catastrophically fail once the strength limits are reached. The CI-CNT material to be used in this stent research, however, differs from typical ceramics, most notably in its mechanical strain behavior. According to Fazio et al., the CI-CNT material has maximum strain capabilities of around 2.3% [21], which is comparable to other compliant materials, including polypropylene, polysilicon, and SU-8 photoresist. Coronary stents, while not MEMS devices, have similar dimensions and deflections. Figure 1.4 shows an example of the types of complex geometry possible with this CI-CNT fabrication process.

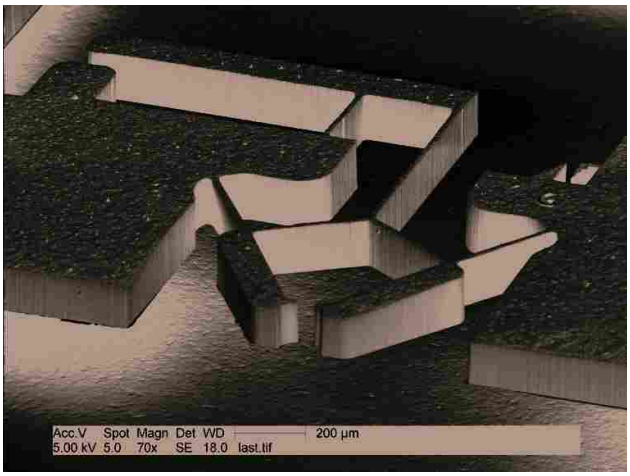

Figure 1.4: Compliant gripper depicting complex geometry from CI-CNTs [21]

1.2 Research Motivation

While it is desirable to avoid any form of angioplasty or stent implantation altogether, these procedures are still necessary under certain circumstances and are therefore still widely used. Because there are relatively few alternatives to these percutaneous coronary interventions, the procedures are performed even with every risk and anticipated side effect, most notably restenosis and thrombosis. Drug eluting stents have been successful in reducing thrombosis compared to bare metal stents [13, 22]. However, it seems that after the drug fully dissolves, the likelihood of thrombosis increases [15, 22]. To combat restenosis and thrombosis, these patients also must indefinitely take blood thinning or anti platelet medication; this includes recipients of drug eluting stents. Many of these issues could potentially be further reduced or eliminated completely by introducing a stent fabricated from material which is more biologically inert. The number of patients needing additional surgical treatment directly related to failed or expired initial stenting could decrease. Fewer procedures directly translates to fewer risks and lower costs. Even with these potential benefits, it seems that little exploration into the use of stents made from biologically compatible ceramics has been published. Significant challenges exist for the design of stents from ceramics. Most notably, compliant, expanding and contracting mechanisms made from ceramics can be difficult to design because of their brittle, fracture-prone characteristics.

1.2.1 Research Objectives

The objectives of this research are:

1. Determine process methods and parameters for CI-CNT material to be used in compliant stent-like structures.

2. Evaluate approximate material properties, including strain expectations for CI-CNT stent devices.

3. Design planar mesh pattern(s) based on previously tested material properties and build analytical model(s).

4. Test planar mesh pattern(s) and compare with analytical model for expected results and to demonstrate potential use of CI-CNT material in stent applications.

1.3 Thesis Outline

This outline describes the flow of the chapters as included in this thesis. Chapter 2 discusses a preliminary effort on the design of planar stent-like geometries using a modified CI-CNT fabrication process. It demonstrates the ability of the geometries to deflect as would be necessary for a stent. Further, it explores the testing and results of these geometries and validates the general plausibility of fabrication of such a design. Chapter 3, like Chapter 2, again demonstrates the capability of CI-CNT material for use in stent applications with planar stent geometries. It however uses data obtained from the work in Chapter 2 to guide the optimal design of three flexible geometries. Additionally, it applies the optimized designs in a cylindrical configuration finite element model. Chapter 4 presents thesis conclusions and describes recommendations for further research regarding CI-CNT material and fabrication process.

CHAPTER 2. FABRICATION AND TESTING OF PLANAR STENT MESH DESIGNS USING CARBON INFILTRATED CARBON NANOTUBES[1]

This chapter explains the fabrication process to create planar stent mesh geometries out of pyrolytic carbon using microfabrication techniques. It further discusses the tests and results used to demonstrate the material's ability to function appropriately in stent-like geometry and evaluate the material properties. This chapter was submitted to the Journal of Nanotechnology in Engineering and Medicine and is presented here with only minor modifications.

2.1 Abstract

In this chapter, we explore and demonstrate the potential of using pyrolitic carbon as a material for coronary stents. Stents are commonly fabricated from metal, which has worse biocompatibilty than many polymers and ceramics. Pyrolytic carbon, a ceramic, is currently used in medical implant devices due to its preferrable biocompatibility properties. Micro-patterned pyrolitic carbon implants can be created by growing carbon nanotubes, and then filling the space between with amorphous carbon via chemical vapor deposition. We prepared multiple samples of two different stent-like flexible geometry designs and smaller cubic structures out of carbon infiltrated carbon nanotubes. Tension loads were applied to expand the samples and we recorded the forces at brittle failure. The cubic structures were used for separate compression tests. We then used these data in conjunction with a nonlinear FEA model of the stent geometry to determine Young's modulus and maximum fracture strain in tension and compression for each sample. Additionally, images were recorded of the mesh samples before, during, and at failure. These images were used to measure an overall percent elongation for each sample. The highest fracture strain observed was 1.4% and Young's modulus values confirmed the the material was the similar to that used in previous carbon infiltrated carbon nanotube work. The average percent elongation was 86% and reached as high

[1]This chapter was submitted to the 2013 ASME International Design Engineering Technical Conference and the Journal of Nanotechnology in Engineering and Medicine at the time of writing.

as 145%. This exceeds a typical target of 66%. The material properties found from compression testing show less stiffness than the mesh samples; however, specimen evaluation reveals poorly infiltrated samples.

2.2 Introduction

A stent is a flexible, tubular mesh which physicians surgically insert into the passages of the human body for purposes including the reduction of localized flow constriction and supporting a collapsed passageway. Stents are used in multiple applications throughout the body and for each application, various stent designs have been implemented [23]. A stent is a compliant mechanism, which depends on flexible members rather than rigid-body joints to achieve motion. Compliant mechanisms have seen significant use in small mechanism research for many years [24]. Specifically, stents are designed to be relatively small for insertion, but capable of expanding once inside the body. When using compliant elements, material selection is crucial, since the device must be designed around the material's maximum stress and strain.

Stents were initially made from stainless steel, a material known to resist corrosion and also capable of tolerating high stress, even plastic deformation, without fracture. For many engineering applications, stainless steel is an appropriate choice because of its strength, well-understood and repeatable properties, and reasonable cost. However, it may not react as well as other materials, namely ceramics and polymers, with the body in biomedical applications [8]. To improve biocompatibility, metallic, ceramic, and polymeric coatings are used with some success [8, 25]. To the body, stents are foreign objects and materials which are therefore acted upon by the body's various methods of defense, causing known stent problems including restenosis and thrombosis. In stent implantation, restenosis is seen as tissue grows from the artery wall onto and over the stent as an immune system response to protect the body. Over time, this tissue begins to hinder blood flow [10]. Another common problem is thrombosis, which is the formation of a blood clot which further restricts blood flow. While restenosis can increase the risk of thrombosis, it is also possible for a stent to cause thrombosis without first experiencing restenosis. Thrombotic events remain the primary cause of death after percutaneous intervention has been performed [11]. Fortunately, materials with improved bicompatibilty have been disovered and engineered [16]. Many of these materials fall in the category of ceramics. Pyrolytic carbon (also known as pyrolytic graphite)

is one such engineered material which the body typically accepts [26]. According to [15–17], carbon and carbonaceous materials are generally well tolerated by animal cells and are therefore commonly used in medical implants. Pyrolytic carbon has been used in such applications as finger joint replacement implants and heart valve replacements [18]. It is not uncommon to design a biomedical device constructed from steel or titanium because of their superior mechanical behavior, but coat the implant in pyrolytic carbon to keep the body from adversely reacting to the bare metal [17]. Pyrolytic carbon is a manmade material that can be created using, among other methods, chemical vapor deposition (CVD), a process commonly used for MEMS fabrication.

Research at Brigham Young University has led to a new method for fabricating systems on the micro and meso scales, including compliant MEMS, using carbon nanotubes (CNTs) [19]. Carbon nanotube-templated microfabrication (CNT-M) is achieved by patterning a growth catalyst on a substrate and growing a forest of vertically-aligned CNTs on top of that pattern. The voids between the CNTs are then filled, or infiltrated, with a material to form a solid structure using CVD. While much research has focused on the remarkable material properties of CNTs themselves, we use them as a physical framework for the infiltration material. Because the volume of CNTs is orders of magnitude below that of the filler material, the resulting properties of the infiltrated structure are primarily determined by the infiltration material. We can fill these voids with amorphous carbon, creating a carbon-infiltrated carbon nanotube (CI-CNT) material. Because the infiltrated carbon is pyrolytic carbon, the structure as a whole becomes a pyrolytic carbon structure. As shown in [21], initial experiments with carbon deposition have shown that carbon-infiltrated structures exhibit a remarkable degree of compliance and strain in bending, where tension is the typical failure mode. The high strain and superior biocompatibility marks CI-CNT as a potentially appropriate and even superior material to typical steels and alloys for stent fabrication.

In order to better understand the ability of pyrolytic carbon to function in stent applications, we designed flexible planar stent meshes as well as simple cubic structures. These designs were fabricated using the CI-CNT process, largely as outlined in [21], with modifications unique to the samples in this study. We then tested the mesh and cube samples to demonstrate flexibility characteristics and a modulus of elasticity was calculated to validate each sample's material properties.

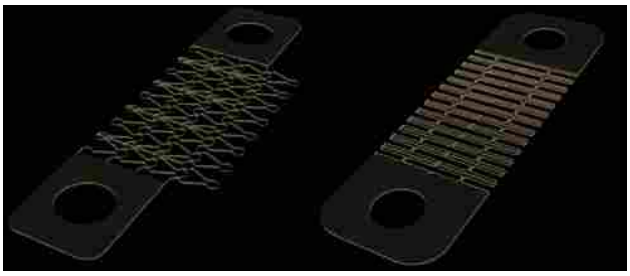

Figure 2.1: Sample mesh designs configured to undergo large deflections

2.3 Procedure

2.3.1 Test Pattern Design

The purpose of the sample meshes was to create a first iteration design to solidify process parameters and methods. These designs were also to be of the general size and shape of current stent geometries in order to demonstrate the ability to flex and deflect in the way a stent would on the same scale of force and displacement. As discussed above, stents are tubular devices made to be inserted into channels or enclosed passageways and, by expanding, can hold the collapsed passageway open. The processing required to fabricate cylindrical CI-CNT structures is still under development. However, much can be learned and demonstrated with stent designs fabricated in a planar configuration. The designs in this study were created as planar versions of flexible meshes that could also be implemented successfully in a tubular configuration.

In addition to the mesh designs, we fabricated small cubes for additional testing purposes and infiltration comparisons. In [21], the author performed much work to quantify material properties as tested in tension, with the CNTs aligned in one direction. Under the assumptions that the CI-CNT material is isotropic, these properties would be identical with CNTs oriented differently. Further, ceramics commonly perform better in compression than in tension. While the properties given in [21] were used as a baseline for design in this work, the cmall cubes were tested in compression to better understand the material behavior in compression.

As noted in [27] and [28], coronary arteries affected by plaque can have diameters reduced to 1 mm, a 66% decrease from a healthy artery diameter of about 3 mm. Typical metal stents are designed and fabricated such that they can be inserted into a small passageway and, once in position, are then expanded by a balloon, plastically deforming to the open or expanded configu-

ration. Because the CI-CNT material is similar to a ceramic, it exhibits a low ductility [21]. We can, however, take advantage of the elastic properties and relatively large strain capability of the material, and design stent meshes in the "large" size as fabricated, and elastically compress them to the "small" size for insertion into the body. Once in the body, the stents could then be released to their initial, as-fabricated size. Using compliant mechanism theory, two designs were created to achieve the 66% change in size using long, thin segments and rounded corners to minimize stress concentrations. These designs are intended to distribute the stress along larger segments of the material, rather than focusing the stress on a single location and creating a weak point incapable of handling large deflections. Figure 2.1 illustrates the sample designs which were fabricated out of CI-CNT material.

To validate our designs before the process of CI-CNT fabrication, large versions were created using a planar laser cutter and acrylic material. We felt the acrylic was an appropriate representation of the CI-CNT material because of its brittleness and tendency to shatter when undergoing large deflections. We successfully prototyped the acrylic designs and demonstrated their ability to flex as required sufficiently to move forward with CI-CNT samples.

The mesh pattern design was used to create a full-size, darkfield photolithography mask for use with a 4-inch wafer and positive photoresist. Multiple instances of the pattern were arranged to make effective use of the entire mask and wafer area.

2.3.2 Fabrication

We followed the same general CNT-M fabrication process as used in [19] and [21], with the appropriate modifications made to the procedure to infiltrate the sample with carbon instead of silicon. The process is described below and illustrated in Figure 2.2 .

Using standard 4-inch silicon wafers, a 30-nm layer of alumina (AL_2O_3) was deposited using an e-beam evaporator (a). The alumina serves as a buffer layer to prevent diffusion of the iron layer into the silicon at the elevated CNT growth and infiltration temperatures. Following the alumina deposition, we used standard photolithography procedures to pattern AZ-3312 positive photoresist on a silicon substrate using a single full-size photolithography mask (b). Then, a 7-nm layer of iron was deposited using a thermal evaporator (c). The iron layer serves as the catalyst for CNT growth and we chose to use 7-nm based on the research performed in [21] and [20]. The

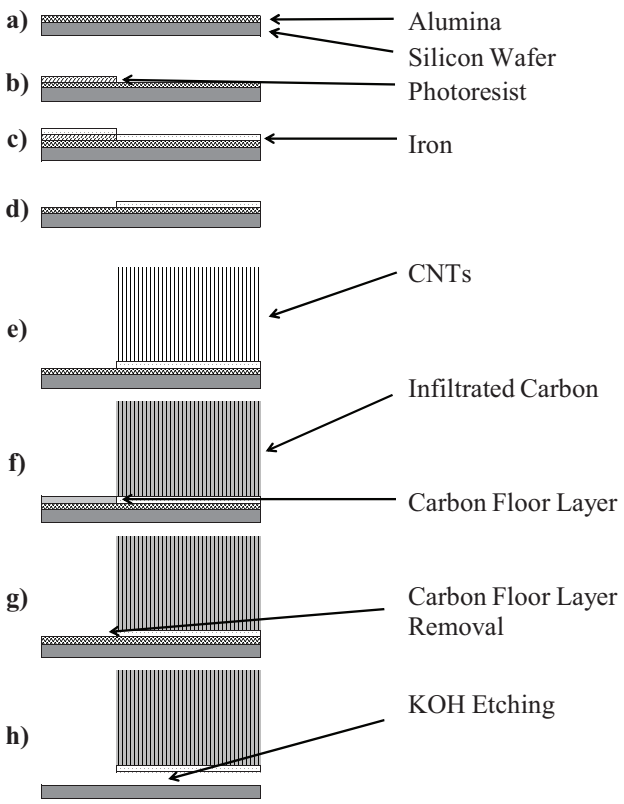

Figure 2.2: CNT-M process with carbon infiltration

final catalyst pattern was obtained by sonicating the patterned wafer in liftoff agent to remove any remaining photoresist (d). We then diced the wafers into four individual pieces appropriately sized for the furnace.

The CNTs were grown and infiltrated with carbon using a CVD process (e) and (f). Samples were placed in a 1-inch quartz tube furnace and heated from room temperature to 750 C in about 15 min while flowing H_2 at 218 sccm. Once the temperature reached equilibrium, 275 sccm of C_2H_4 was added for 30 minutes to grow the carbon nanotubes. After 30 minutes, the C_2H_4 was switched off and the furnace was allowed to ramp up to the infiltration temperature of 900 C. Once the furnace had reached the new equilibrium temperature, 327 sccm of C_2H_4 was again added, and infiltration via CVD commenced. Infiltration lasted for 30 minutes. When infiltration was complete, the furnace was shut off, but not opened, thus allowing the samples to cool slowly to around 650 C. Once this temperature was reached, the furnace was opened and samples allowed to cool much faster to a temperature appropriate for handling. We then removed the samples from

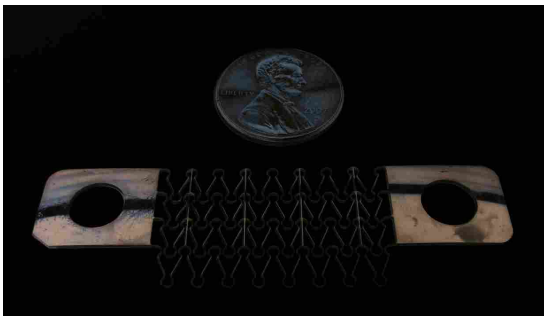

Figure 2.3: Example of sample size comparison to a United States penny

Figure 2.4: Sample mesh example after KOH release and rinse

the furnace. Slight intrinsic stresses on the large end "pads" of the samples resulted in the pads self-separating from the silicon substrate, likely during cooling.

To effectively separate the delicate samples from the substrate, additional processing was required, namely, a number of etching processes. The CVD process creates a floor layer of carbon on the substrate surface where CNTs were not grown. We removed the carbon floor layer using a planar dry etching machine flowing O_2 and setting the generator power to 200W for a duration of 5 minutes (g). To fully remove the carbon floor layer, this dry etch process was repeated 3-5 times until the shiny surface of the silicon substrate was visible through the sample's infiltrated CNT structure. With the alumina exposed, KOH was used to wet etch away the alumina and silicon until the samples were released from the substrate. We placed the samples in a bath of KOH solution heated to 100 C and etched for approximately 30-45 minutes, or until the infiltrated CNT samples had visibly detached from the substrate (h). Once the sample was released, it was removed from the KOH bath, rinsed with room temperature distilled water, and dried accordingly. Note that once the sample had released from the substrate, extreme care was taken in handling the sample to minimize any sample breaks or fractures before testing. An example of a completed sample is shown in Figure 2.3 and more detail in Figure 2.4.

2.3.3 Testing Procedure

Each mesh sample was tested in an Instron tabletop tensile testing machine, using specially machined fixtures attached to a force transducer to gradually expand the stent mesh and record the resulting force. The large pad and hole at the ends of each sample were used to secure the sample

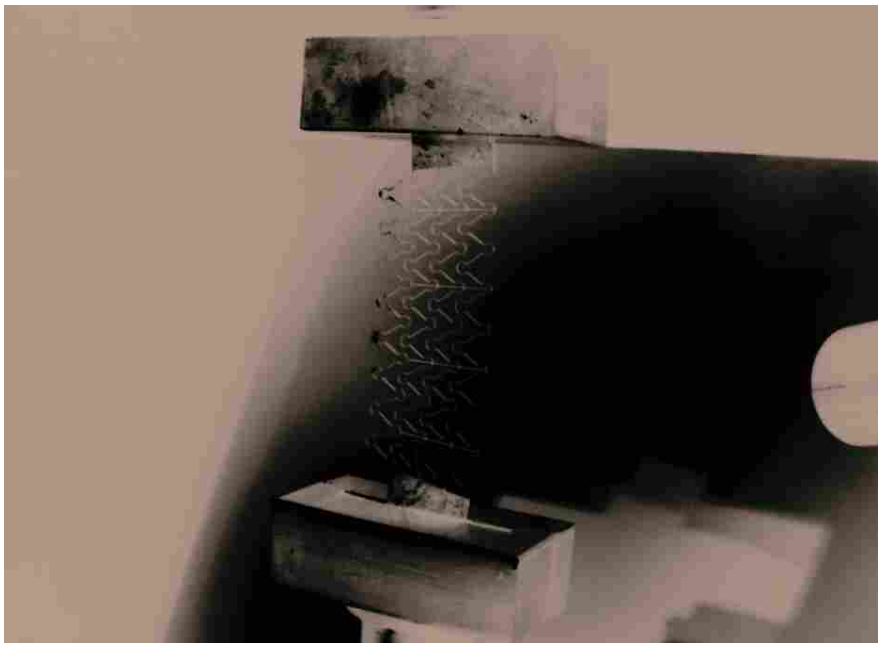

Figure 2.5: Planar mesh test setup in the Instron and gripping fixtures

in the special fixtures while minimizing any stress concentration or effect of the clamping system on the delicate samples. The fixtures were machined each with a male and female half. The male half was secured to the tensile machine with an exposed post, through which a sample could be threaded, and the female half placed over the sample and male half, thus ensuring that the sample did not detach from the testing apparatus. The hole and shaft configuration also allowed the sample to slightly rotate, if needed, during expansion, to find the natural position of lowest energy, rather than attempting to manually set this position. Using a high resolution camera fitted with a zoom lens, we observed and visually recorded each test. Figure 2.5 shows how the testing equipment and samples were arranged.

We tested each mesh sample individually by placing the unstretched mesh structure in the fixtures and expanding the sample at a constant rate of 0.5 mm/min until fracture occurred. Deflection and force values were continuously recorded as well as picture capture at a rate of 5 frames per second during each test. Following each expansion test, the data were copied from the testing program into a spreadsheet. We saved initial, unstretched frames and frame-before-fracture images from the camera for expansion measurements and test videos of each sample were compiled.

Cubic structures were tested with a similar tensile testing machine, but in a compression environment. The millimeter-sized cubic samples were placed in between two flat-ended fixtures which were themselves clamped in the tensile machine's hydraulic gripping jaws. Each flat-ended fixture was machined out of hardened steel to minimize deflection resulting from the fixtures themselves. We compressed the cubic samples at a rate of 3μm/min with CNTs oriented both in line with the compression load, and transversely oriented. Following each compression test, the data were compiled from the testing program into a spreadsheet.

2.3.4 Data Analysis

As stated above, the purpose of this effort was to demonstrate the ability of C-CNTs to flex and deflect as would be necessary for a stent of similar shape and size and validate material properties as noted in [21] using stent-like geometry. The cubic compression samples were fabricated and tested to obtain raw material properties. These material properties could be easily taken from the raw compression data due to simple cubic geometry. Because the complex mesh geometry being tested was not a simple, constant cross-section beam, we could not use the Instron force data to directly find a modulus of elasticity of the material, the strain, or the ultimate strength. Instead, a model was created in ANSYS to simulate each test independently of one another for both stent designs.

We constructed a single "cell" from each flexible design's array of repeated cells in the ANSYS simulation environment. Using PLANE183 elements, planar geometries with a constant thickness were created. One end of the simulation cell was fixed while the other was allowed to move according to the images captured during testing. The images recorded during testing were used to find the deflection values for each test. For each sample, the unstretched and frame-before-fracture images were loaded into a CAD software drawing environment. Once loaded, we measured the initial, unstretched single cell and the same deflected cell on the pictures using the software dimensioning tools; the deflection value was found by finding the difference between the two measurements. Examples of these images are shown in Figure 2.6. To obtain the true dimensioned values, rather than a value skewed or scaled by the camera or dimensioning software, a reference dimension was also taken in the CAD drawing environment whose actual dimensions were measured using a digital microscope. Together with the reference dimension, the actual cell

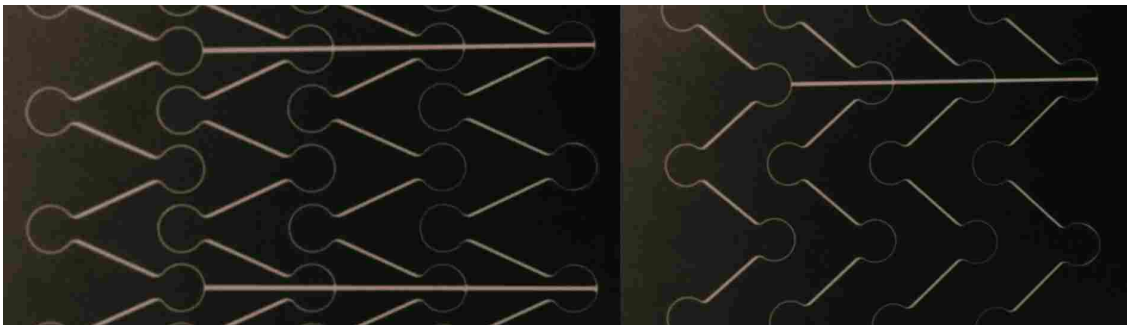

Figure 2.6: Camera view sample of images where measurements of deflection were taken

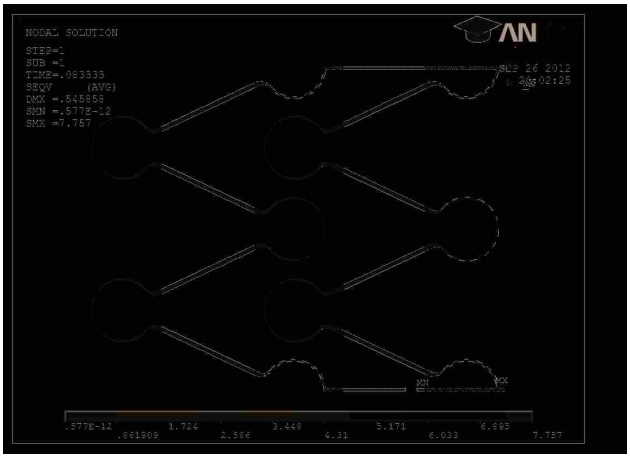

Figure 2.7: One of the mesh design simulations in the ANSYS environment

displacement was calculated and applied to the model in ANSYS. Figure 2.7 shows one of the mesh design simulations in the ANSYS environment.

In addition to the known displacement, the force at the maximum displacement was continuously recorded by the Instron machine. Because the sample mesh designs were configured in a "serial" pattern, the same force applied in each individual section of the design. Within each individual section undergoing the same force, a number of cells were configured in a "parallel" pattern. Each cell and section could be analyzed similar to a system of serial and parallel springs. By taking the measured maximum force from each test, we could then adjust it according to the specific geometry being in parallel or series that was simulated in ANSYS. This adjusted force then became the target for the ANSYS simulation. For each test, an initial guess for Young's Modulus was given and ANSYS was allowed to iteratively solve the simulation, changing the Young's Modulus until the resulting reaction force matched that which was measured with the Instron. In

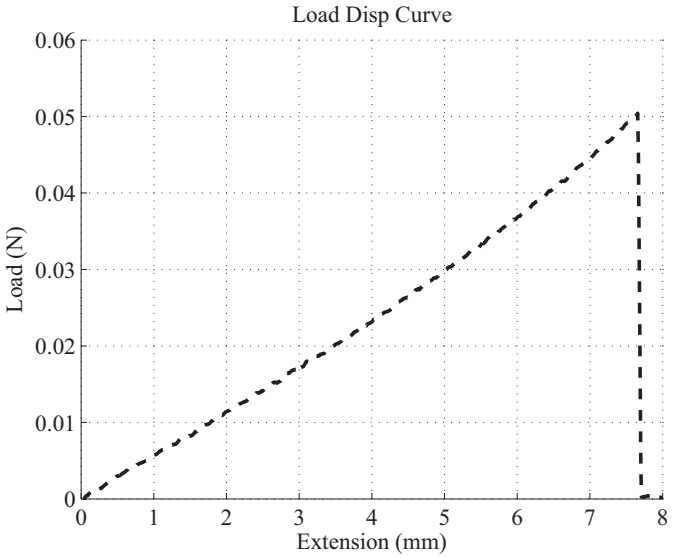

Figure 2.8: Typical Force-Deflection curve for the stent mesh tensile samples

addition to Young's Modulus, we were also able to obtain maximum values for stress and strain from the ANSYS simulations.

2.4 Results and Discussion

Figure 2.8 shows a typical force-deflection curve for the CI-CNT mesh designs. As mentioned previously, the plot reveals that the curve is nearly linear and additionally, samples do not exhibit plastic deformation before failure. This translates to a linear stress-strain relation for the material up to failure. The sudden drop of force back to zero indicates that failure is characteristic of an instantaneous, brittle failure.

Figures 2.9 and 2.10 show the simulation calculated values of maximum strain and Young's Modulus for each sample tested and Figure 2.11 shows the percent elongation for analyzed cells. For stents, which rely heavily on the compliance of the material to function properly, a high maximum strain is desirable. High strains translate to greater deflection before failure. The highest average strain measured in this stent pattern experiment was greater than 1.4% while the lowest average strain value measured was 0.4%. Modulus calculations had a similar range of values. The highest average modulus calculated was close to 15 GPa while the lowest was close to 5 GPa.

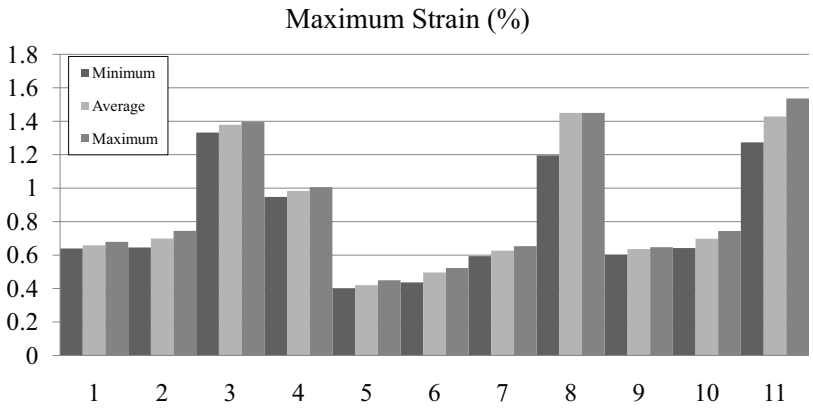

Figure 2.9: Strain values as calculated from the ANSYS analyses

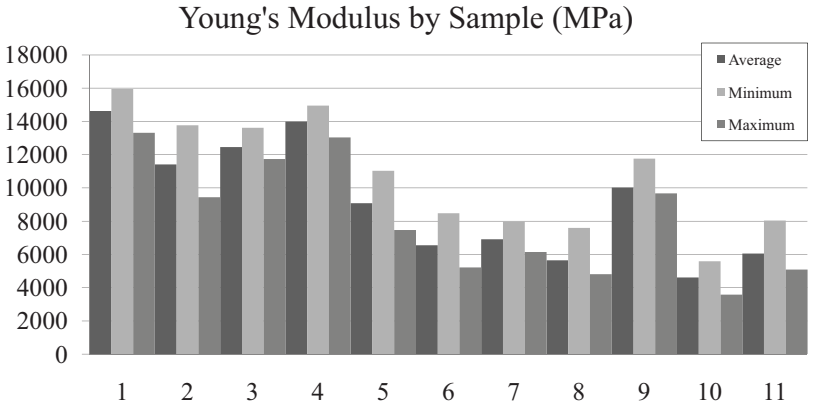

Figure 2.10: Modulus values as calculated from the ANSYS analyses

Percent elongation to failure values were consistently above 45%, with only two samples failing to reach the 66% elongation target and one sample reaching approximately 145%.

In the figures showing values for average modulus and strain, there is also data representing a maximum and minimum. These values came from the variability in the beam's physical dimensions. The critical flexible segments were designed to be a certain size, but upon investigation and measurement with a digital microscope, it was found that the beam width was not as designed. In some cases, the difference was as large as 30%. Additionally, we found that actual beam width varied on each sample. Approximately 30 measurements were taken for each sample and from them, an average, maxiumum, and minimum beam width was calculated. These values were then used to reanalyze the data, resulting in a modulus and strain range for each sample.

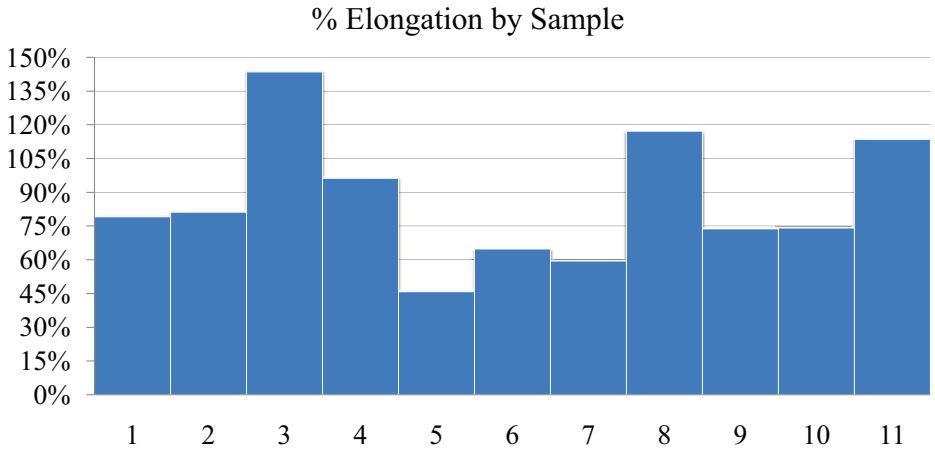

Figure 2.11: Percent elongation of each analyzed test cell

Figure 2.12 shows a summary of all cubic samples' tests in compression. The light lines indicate samples whose CNTs were oriented transversely to the load while dark lines indicates CNTs aligned the the same direction as the load. As loading began, both the transverse and aligned samples had the same Young's Modulus. At some point, however, the aligned samples underwent a change to a reduced Modulus, as shown by the dark lines suddenly continuing along a differend slope. The highest ultimate strength was about 190 MPa while Young's Modulus was evaluated to be 1.4 GPa, and for samples that underwent a change, 290 MPa for the second modulus. It was also interesting to note that the orientation seemed to affect the way each sample failed in compression. If the sample was loaded transversely, fracture occured so quickly and completely that remnants of the samples could hardly be recovered. If the sample was loaded aligned with the CNTs, it went through a slow material separation, effectively "smashing" into a powder rather than fracturing.

Even though each mesh sample performed largely as anticipated, we can see from the results that a large amount of variability is present in the data. After conducting the experiments, we feel there were some major factors contributing to the variation. First, these tests were completed over a relatively long period of time so that they are affected by process variation over time. More specifically, each machine or piece of equipment used was likely affected by other experiments or work using the same machine. Second, the photomask itself, being made as an emulsion-based transparency mask, had line edges that degrade over time. These degraded edges lead to rough surfaces on the samples and stress concentrations where the sample would fail at lower stresses. Third, the samples were designed to have a large number of cells throughout the entire mesh.

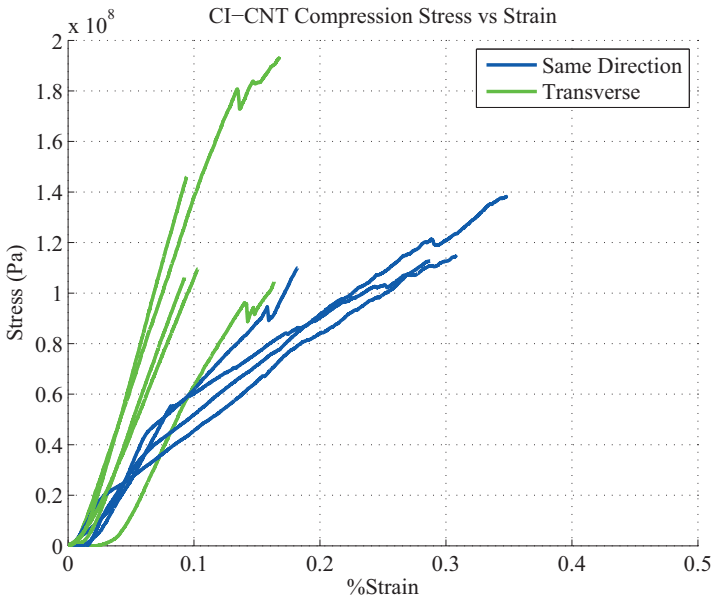

Figure 2.12: Plot showing compression samples with CNTs aligned in both directions

Only one or two of the cells could be capture in the view area of the camera and analyzed. It is possible that sample failure on some samples occured somewhere on the mesh outside of the images being viewed. While the same force was felt throughout the sample, some sections or cells, due to geometric inconsistencies, may have undergone larger deflections. If this is the case, these sections would fail before the imaged section, and affect the results as simulated in ANSYS.

Upon further investigation of the cubic compression samples, it was found that infiltration likely caused the drastic reductions in Young's Modulus. Figures 2.13 and 2.14 show the same compression sample after fracture. Due to the relatively large (1 mm cube) nature of these cubes, the amorphous carbon did not penetrate fully throughout the forest of nanotubes under the infiltration parameters used for the flexible meshes. While no exact density measurement was taken, the images in Figure 2.13 and Figure 2.14 show voids in the structures' composition which are not present on SEM images of the much smaller structures.

2.5 Conclusion and Recommendations

An experiment was conducted to validate the potential capabilities of the CNT-M process to create stent-like geometry of the same shape and size as stents currently on the maket. Once the

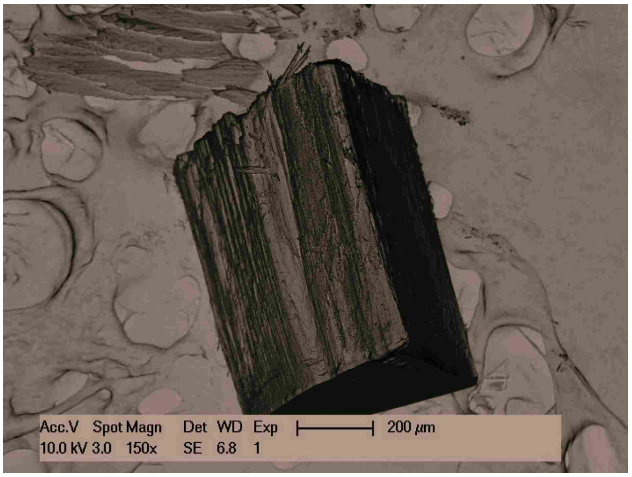

Figure 2.13: SEM image of broken transverse compression sample

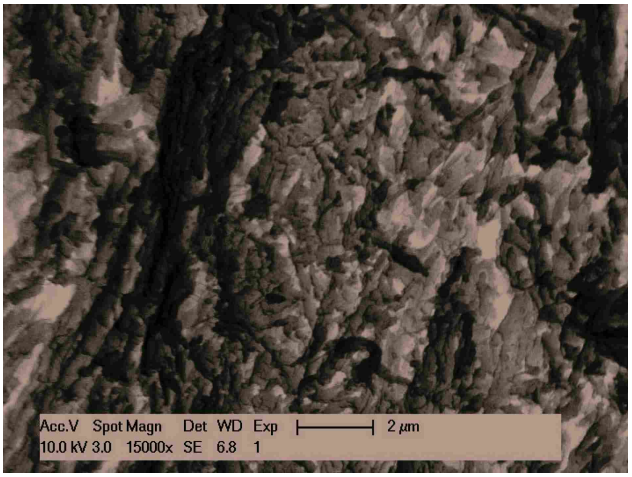

Figure 2.14: SEM image of broken transverse compression sample with detail on infiltration quality, revealing multiple voids in the material

structures were fabricated, they were tested in tension to demonstrate the material's flexibility and measure strain values. In addition to the measurement of strain values, Young's modulus was also measured/calculated to confirm the material as pyrolitic carbon. Next, the percent elongation of individual cells were measured. We found that stent-like structures composed of pyrolitic carbon, as fabricated using the CNT-M process, will deflect sufficiently, even in excess of the target 66% elongation, without fracturing and could therfore potentially be used in such applications. Lastly, even though the cubic compression samples were a poor representation of the material for gathering compression properties, an ultimate strength of 190 MPa was still achieved, which is slightly higher

than the maximum ultimate strength of 181 MPa found in mesh sample tension tests. This suggests that the material is potentially stronger in compression.

While this research performs a similar exploration into the material properties of the CI-CNT material as discussed in [21], the load orientation on the material was different. Due to the volumetric dominance of infiltrated carbon in these structures, we expect loading in every direction, regardless of CNT orientation, to produce similar results. However, it is possible that the presence of CNTs may cause slight inconsistencies between values reported in this work and that of [21] as introduced by the compression testing in this work. A useful study would be the investigation and quantification of the CI-CNT material's anisotropy. As processing techniques for cylindrical fabrication become available, the CI-CNT material could be a potentially interesting choice for arterial stents.

2.6 Acknowledgement

We acknowledge Clarke Capital Partners for their support and funding in part of this work, as well as the BYU Integrated Microfabrication Lab. We also thank Darrell Skousen for his collaboration in this work.

CHAPTER 3. OPTIMIZED DESIGN AND TESTING OF SEMI-AUXETIC CI-CNT ARTERIAL STENT GEOMETRIES[1]

3.1 Introduction

This portion of the thesis discusses the further evolution of potential CI-CNT stent designs. In this chapter, we demonstrate the capability of CI-CNTs for use in stent applications with planar stent geometries of the actual size and scale for a coronary arterial stent. In the design stage, however, we used data and understanding obtained from the work performed in Chapter 2 to guide the optimal design of two new flexible stent geometries. Existing auxetic patterns were evaluated for possible application in the stent designs. Slight changes were made to the mask design and fabrication processes based on the new geometries, testing considerations, and experience gained during Chapter 2 research. The testing and data analysis are presented and discussed in detail. Additionally, this chapter discusses how the optimized planar designs were applied in a cylindrical configuration finite element model to demonstrate how the planar designs will function as cylindrical devices.

3.2 Design and Optimization

3.2.1 Auxetic Exploration

As discussed in the beginning of this work, arterial stents undergo a large amount of deflection. For existing stents made from stainless steel or other metallic alloys, this deflection happens as the stent is plastically expanded. The brittle properties of CI-CNTs prevent the design of a similar plastically expanding stent. We can, however, take advantage of the relatively high strain and elastic properties of the CI-CNT ceramic and design a compliant stent that is already "expanded" as fabricated, but elastically compressed for insertion into the body. Because many compliant ge-

[1] Much of this chapter will be included in a journal paper submission

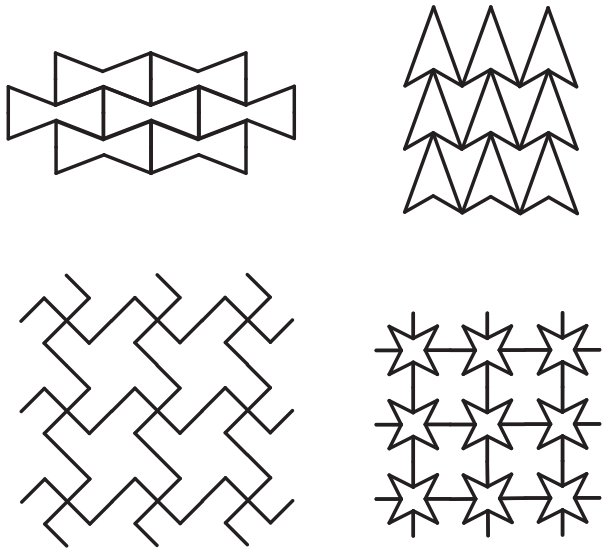

Figure 3.1: Common auxetic honeycombs used to model negative Poisson's ratio materials from [31]

ometries already exist that have been extensively researched and optimized for compression similar to our stent application, we explored these geometries in an effort to find an appropriate starting point for our stent mesh pattern.

One area of compliant designs seeks to model the negative Poisson's ratio phenomenon found in some materials [29]. These materials exhibit the uncommon two and three dimensional characteristic of getting larger when stretched and smaller when compressed [30]. An auxetic stent design would be advantageous in our particular application. Unlike conventional metal stents, the CI-CNT stent would be compressed before insertion. If the stent were an auxetic design, the compression would not only make the device smaller in diameter, but also shorter in length. This is advantageous because overall length of the catheter-balloon delivery system could correspondingly be shorter and therefore easier to maneuver from the arterial insertion location to the affected area. Figure 3.1 shows a few common auxetic honeycombs used for mathematical modeling.

Auxetic materials' low energy or "natural" state is compressed, or small. By applying a force, the auxetic nature of the material is revealed. The reverse is intended for our CI-CNT stent designs. After considering many of the auxetic honeycomb arrays available, the "bowtie" design was chosen because of its relatively simply deflection mechanism. This array is shown in the top left of Figure 3.1. Some of the more interesting auxetic honeycombs relied on more complicated

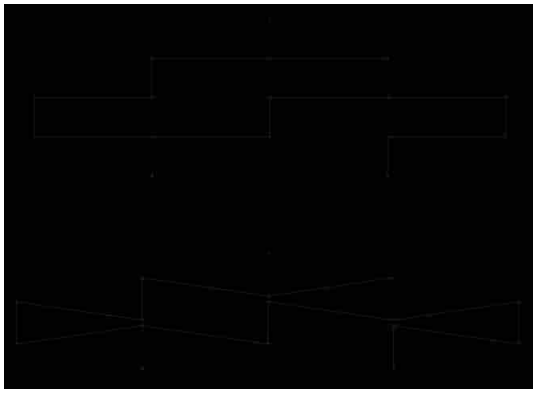

Figure 3.2: Underlying rigid-body skeleton of bowtie honeycomb

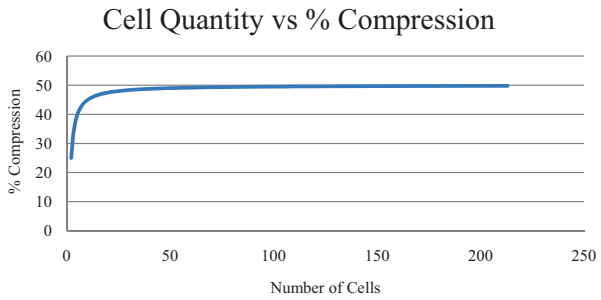

Figure 3.3: Bowtie honeycomb percent compression limit

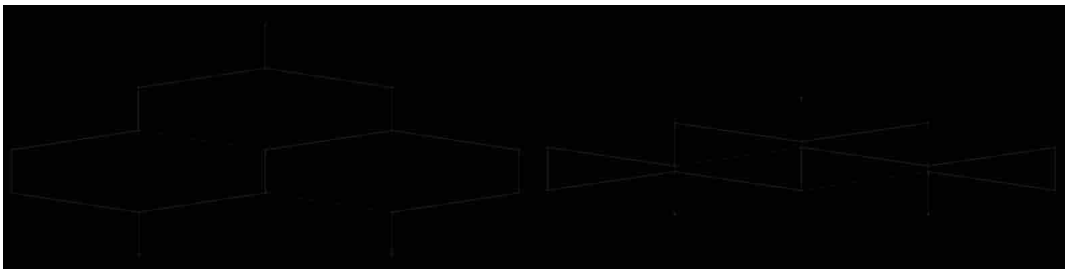

Figure 3.4: The bowtie honeycomb adjusted to allow for high percent compression

deflections which we were not confident the CI-CNT material could undergo. Also, trigonometry revealed that the "bowtie" option gave the a very high percent compression for a given beam deflection.

The bowtie basic design as applied to a stent would consist of an array of flexible, horizontally arranged beams along the length of the stent, and short, rigid beams oriented vertically along the circumfrence of the stent as shown in Figure 3.2. Each repeated set of horizontal beams and vertical rigid segments is called a "cell." As the beams deflect, there is a limit to the distance traveled before the adjacent cell is reached, preventing further deflection. As the number of cells is increased, the percent compression also increases. However, there is a limit to this percent compression as shown in Figure 3.3. Initally, adding more cells results in a dramatic increase for the potential percent compression in the design, but this increase quickly changes and a limit of 50% compression is reached. To attain a 60-63% compression necessary for our stent design using the bowtie honeycomb, we altered the basic pattern slightly. Rather than designing the flexible beams

to be exactly horizontal, they were changed to open slightly outward, as shown in Figure 3.4, which allows us to create a semi-auxetic array capable of percent compressions higher than 50%. It is semi-auxetic in nature because as the rigid beams are compressed toward each other, the honeycomb undergoes a slight expansion initially, then compresses like the original bowtie honeycomb.

3.2.2 Optimization

The adjusted bowtie design provided the basic rigid link pattern to follow for the design of our CI-CNT stent. However, specific beam dimensions based on material properties and compression specifications were necessary. Because the bowtie design is basically an array consisting of the same repeated cell, a properly optimized design of a single cell would optimize the entire array. Further, a single cell consists of four identical beams which undergo the same deflection. Figure 3.5 shows the target geometry required to be optimized. We know from compliant mechanism theory that thinner beams are able to undergo larger deflections with lower stresses [24]. The horizontal beams needed to be thin and flexible while the vertical beams remain thick and rigid to provide some structure, shape, and support for the stent design. Based on an expanded planar "height" of 3π mm (expanded diameter of 3mm) and a compressed "height" of π mm (compressed diameter of 1mm), we chose certain parameters and others were dependent on those chosen parameters of the adjusted rigid link bowtie model. Table 3.1 highlights these parameters and Figure 3.5 shows them on the basic geometry. Note that the "Number of Cells" and "Cell Half Width" were chosen based on prelimary calculations and experience regarding the deflection capabilities of the CI-CNT material.

Table 3.1: Design Parameters

Parameter	Chosen/Dependent	Design 1	Design 2	Design 3
Number of Cells	Chosen	12	10	8
Compressed Height (mm)	Chosen	3.142	3.142	3.142
Rigid Section Length (mm)	Dependent	.483	.571	.698
Expanded Height (mm)	Chosen	9.425	9.425	9.425
Cell Half Width (mm)	Chosen	2	2	2
Flexible Link Length (mm)	Dependent	2.022	2.034	2.056
Flexible Beam Width (mm)	Chosen	.025	.025	.025

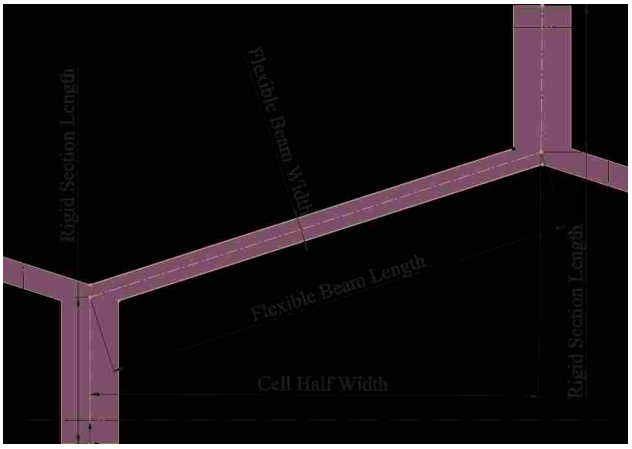

Figure 3.5: Target geometry to be optimized

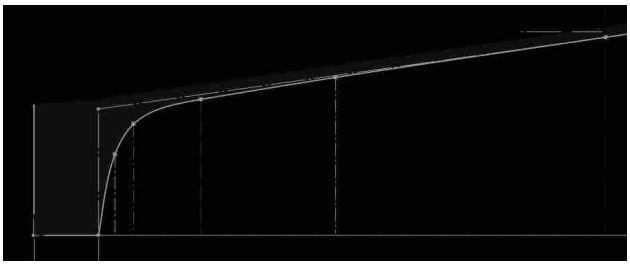

Figure 3.6: Image showing the spline control points

For each of the given potential designs listed in Table 3.1, a deflection analysis could be performed to provide stress and strain values. However, these parameters do not include a consideration for the corner stress concentration of the beam geometry. This is obviously where the highest stresses would occure. Placing a typical fillet in the corner is a common way to reduce the effect of the stress concentration. Even more effective than a simple constant radius fillet would be a tapered flexible beam in combination with a non-constant radius fillet. In other words, rather than designing the corner geometry with a line, a constant radius arc, and another line, we could design the geometry with a spline. This spline would also need to be optimized for stress distribution through the material rather than at a single location.

Using the optimizer in ANSYS, we created a routine which took the parameters listed in Table 3.1 and built the appropriate geometry. For spline creation, we chose four horizontally spaced locations where spline control points could be placed. These control points were restricted horizonally at specific locations but allowed to move vertically, thus dictating the shape of the

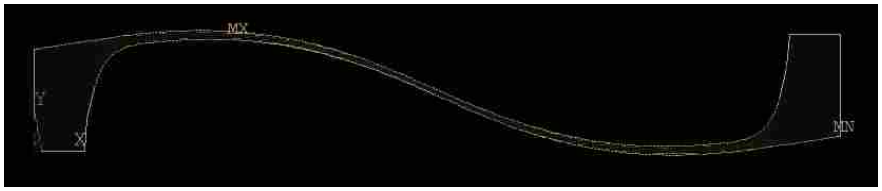

Figure 3.7: Example of optimized taper with deflection and stress plot

Table 3.2: Optimized Taper Stress at Max Deflection (10 Cell) (MPa)

		Beam Width (μm)					
		25	23	21	19	17	15
Half Cell Width (mm)	1.5	289.45	288.9	259.82	251.28	242.75	233.77
	1.75	204	193.73	188.13	179.6	164.6	157.7
	2	156.09	144.9	139.67	136.88	127.8	117.35
	2.25	120	113.78	107.8	101.17	95.17	86.88
	2.5	95.35	90.01	85.41	80.5	75.07	71.6

spline. Figure 3.6 shows an example of how the spline control points are located with respect to the beam geometry. The ANSYS routine built the geometry with a user specificed set of spline control points, performed the deflection and stress analysis, and using gradient based optimization, would change the vertical component of each spline control point and perform the analysis again until an optimum was reached. In order to fully explore the design space, we allowed the cell half width and flexible link width parameters to incrementally be adjusted to higher and lower values. The results of the ANSYS optimization routine for the 10 cell design can be seen in Table 3.2. Similar tables for the 8 Cell and 12 Cell designs can be found in Appendix A.1. Figure 3.7 shows an example of how ANSYS was able to sucessfully optimize a spline geometry within the given parameters and constraints to minimize and distribute stress along the beam material. Note that in Figure 3.7, the maximum stress has moved away from the initial "corner" where the rigid section transitions to the flexible beam.

To validate the optimization results that ANSYS provided, we plotted stress vs beam width and stress vs half cell width. These plots are shown in Figures 3.8 and 3.9. For a simple cantilever beam, stress varies linearly as the beam width is increased and varies with the third power of beam length, which is essentially how changing the cell width affects the beam. As shown in the Figures,

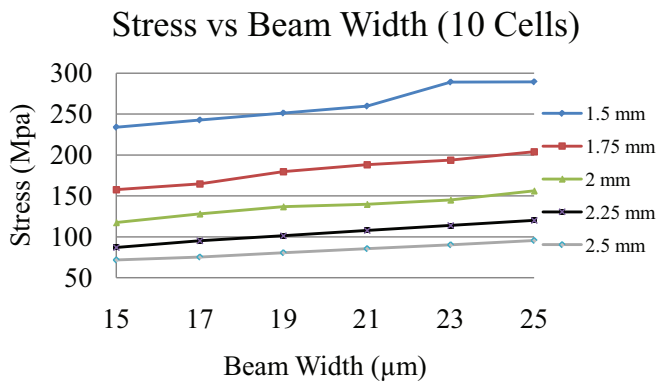

Figure 3.8: Stress vs beam width of the 10 Cell spline optimization results

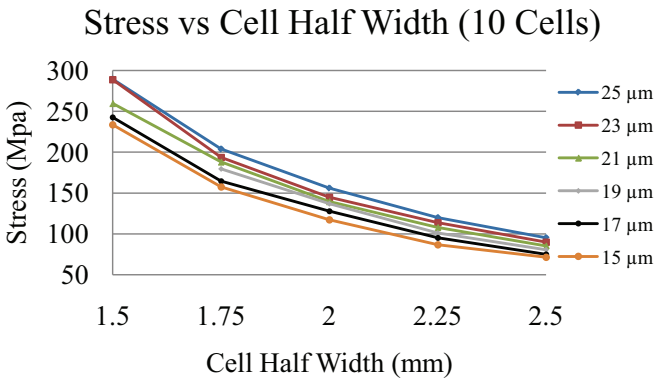

Figure 3.9: Stress vs cell half width of the 10 Cell spline optimization results

the changes of beam width and cell half width affect stress as anticipated. Similar validation plots for the 8 Cell and 12 Cell designs can be found in Appendix A.2.

We can see in Table 3.2 that there are multiple optimized designs that can undergo the deflection while remaining near the target stress threshhold of 100 MPa. To narrow our design parameter options, we pulled reaction force data from the ANSYS optimization simulations, and created Table 3.3 which shows the force/stress ratio for each design. Similar tables for the 8 Cell and 12 Cell designs can be found in Appendix B.2. Note that the ratios have been multiplied by a large constant to make them more managable in evaluation. Some of the table values don't have a ratio, but rather the designation "High Str" denoting that the stress calculated by the ANSYS optimization was over a chosen maximum threshold value of 130 MPa. Without knowing exactly what kind of force/stress ratio the stent would need to have, we hypothesized that since most current stents are fabricated from metal, we would want the highest force/stress ratio, or stiffness,

Table 3.3: Optimized Taper Reaction Force/Stress Ratio (10 Cell)(Units Arbitrary)

		Beam Width (μm)					
		25	23	21	19	17	15
Half Cell Width (mm)	1.5	High Str	High Str	High Str	High Str	High Str	High Str
	1.75	High Str	High Str	High Str	High Str	High Str	High Str
	2	High Str	High Str	High Str	High Str	.458	.404
	2.25	.5395	.494	.446	.403	.362	.308
	2.5	.457	.413	.371	.333	.292	.237

possible. While we were able to anticipate that wider beams and thinner cell widths would produce higher force/stress ratios, it was useful to compile these tables to compare different combinations of parameters and stresses. Using the force/stress ratio and stiffness considerations, we chose the following designs as shown in Table 3.4. Due to the apparent variability of material properties as shown in Chapter 2 and [21], we did not choose the designs whose simulated stress was close to the threshhold. This is also why no 8 Cell designs were chosen.

Table 3.4: Chosen Design Parameters

	Number of Cells	Half Cell Width (mm)	Beam Width (μm)
Design 1	10	2.5	25
Design 2	12	2.25	25

3.3 Fabrication and Testing

3.3.1 Mask Design

While the optimization process helped us to design the semi-auxetic structures, the actual mask required further design work. Through the fabrication and testing performed in Chapter 2, we gained additional insight on what features should be added to a mask to improve this process.

The large “pads” present on the samples tested in Chapter 2 were succeptable to instrinsic stresses and in some cases, these stresses were high enough to cause cracking. To combat this, “holes” were placed anywhere there would otherwise be a large surface area of CI-CNTs. These holes were carefully sized and placed to not affect the functionality of the stent geometry. These

holes were also intended to reduce the KOH etching time required to release the structures from their substrates. This mask also included support structures as mentioned in [19]. We also learned during Chapter 2 research that the support structures included on a mask design intended to help the CNTs grow straighter should be relatively small in size and simple in shape. The support structures in our mask were essentially small 150 μm squares spaced 30 μm apart from each other and the flexible beams. Lastly, we considered how the samples would interface with the testing fixture. As will be discussed in Section 3.3.3, the edges of each sample would interface with the fixture to prevent the samples from buckling. We designed for this by including extra material on the outermost rigid segments. Lastly, these planar versions of what would be a cylindrical design included fixed lateral boundaries on the top and bottom edges, where the cylindrical design would not. We designed for this by extending the cell array 2.5 cells beyond the target 10 or 12 cell designs. This was intended to remove the effect of the boundary conditions on the target 10 or 12 cell flexible area. Complete mask designs for the 10 Cell and 12 Cell designs are included in Appendix C.1.

3.3.2 Fabrication

We used essentially the same fabrication method as outlined in Chapter 2 to fabricate the semi-auxetic stent designs. This process is outlined in Figure 2.2 and discussed in detail in section 2.3.2. Rather than altering the fabrication process and possibly changing any process parameters that could potentially affect the CI-CNT material properties, we only changed some of the sample release methods.

In Chapter 2, we discuss in detail the specific steps taken to release the samples from each silicon substrate. Anticipating the same release methods being necessary to release the semi-auxetic stent samples from their silicon substrates, we began the same process beginning with the removal of the carbon floor layer. We again used the planar dry etching machine and flowed O_2 and while setting the generator power to 200W. After two to three five-minute etching cycles, we inspected the samples and found that they were already separating from the substrate. Up to six planar etch cycles were sufficient to etch away enough carbon floor layer and gently separate the samples from the substrate with small forceps. This fortunately allowed us to forego the process

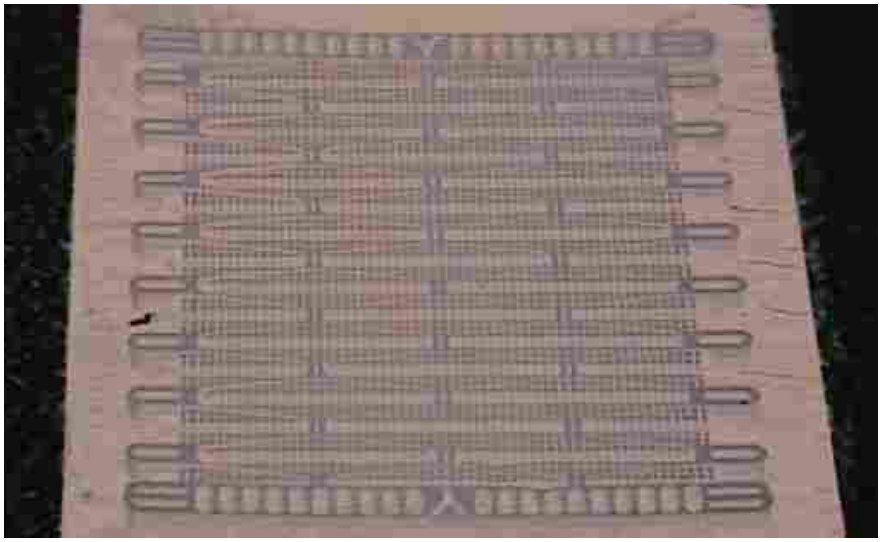

Figure 3.10: Example of stent mesh sample after the furnace CNT growth and infiltration

of KOH etching and rinsing as it is manually challenging and the fluid surface tension is capable of breaking the small samples.

One possible explaination as to why we were able to forego the KOH etching and manage to separate the samples from the substrate was the design of the structure. More specifically, while there were both rigid and flexible segments throughout the geometry, nowhere on the structure was there a "pad" or large area of pure CI-CNTs. In other words, like hollowing out a solid volume to reduce weight, we placed through "holes" througout the design as mentioned in Section 3.3.1. This likely allowed more of the carbon floor layer to be etched away than was possible for the samples in Chapter 2. Figure 3.10 shows a sample after the furnace CNT growth and carbon infiltration.

3.3.3 Fixture Design and Testing Procedure

The testing procedure largely followed that as described in Chapter 2 with adjustments for compression rather than tension testing and the specific changes in sample geometries. We tested each optimized design sample in an Instron tabletop tensile testing machine, using a specially designed fixture and a force transducer to gradually compress the stent mesh and record the resulting force and deflection. The purpose of the fixture was to hold the sample vertical and keep it from buckling during compression while also minimizing friction and surface contact between the fixture and the sample itself. We accomplished this by machining two mating pieces, one fixed to a

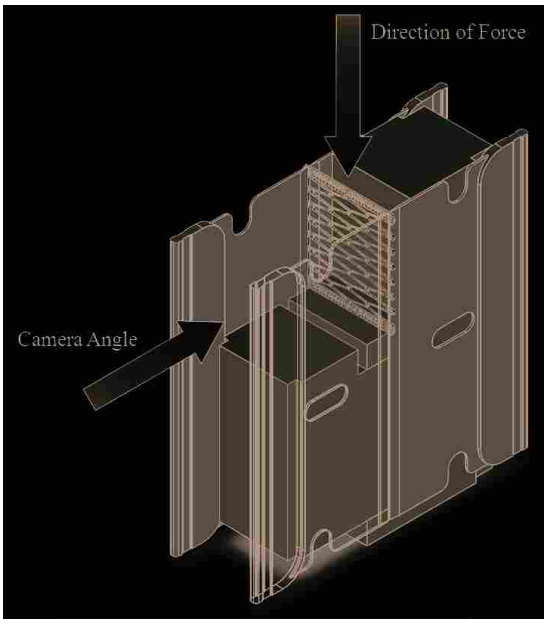

Figure 3.11: CAD model depiction of testing fixture and setup

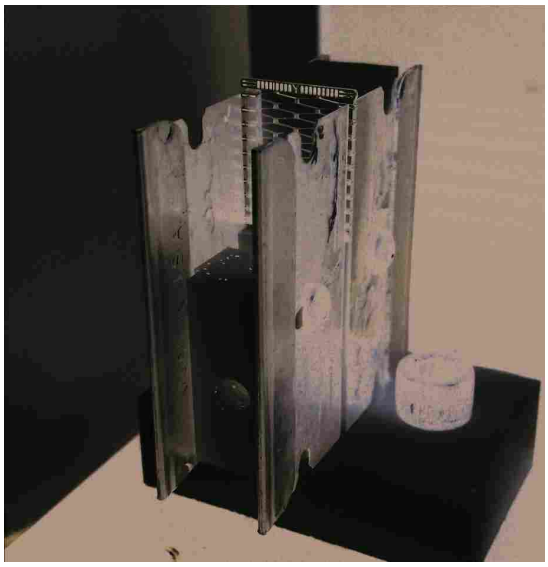

Figure 3.12: Photograph of actual testing fixture in the tabletop Instron

testing stage, with each piece having two razor blades attached, one on each side. The ungrouded fixture piece moved in and out relative to the other by the means of a screw. As we turned the screw, the ungrounded fixture piece and its attached razor blades would separate from the other fixed razor blades, revealing a gap where the samples would be placed. Once the sample was inserted into the razor blade gap, the blades could once again be brought together until minimal contact was made with the sample edges, thus inhibiting any buckling behavior while minimizing frictional and surface contact effects. Using a high resolution camera fitted with a zoom lens, we observed and visually recorded each test. Figures 3.11 and 3.12 show how the testing fixture and setup were arranged.

We tested each stent geometry sample individually by placing the uncompressed pattern in the fixture, securing the sample from buckling and compressing the sample at a constant rate of 3 mm/min until catastrophic failure occured or compression changed from being a funtion of beams deflecting to beams contacting each other and pressing material directly on material. Displacement and force values were continuously recorded as well as picture capture at a rate of 3 frames per second during each test. Following each compression test, the data were copied from the testing

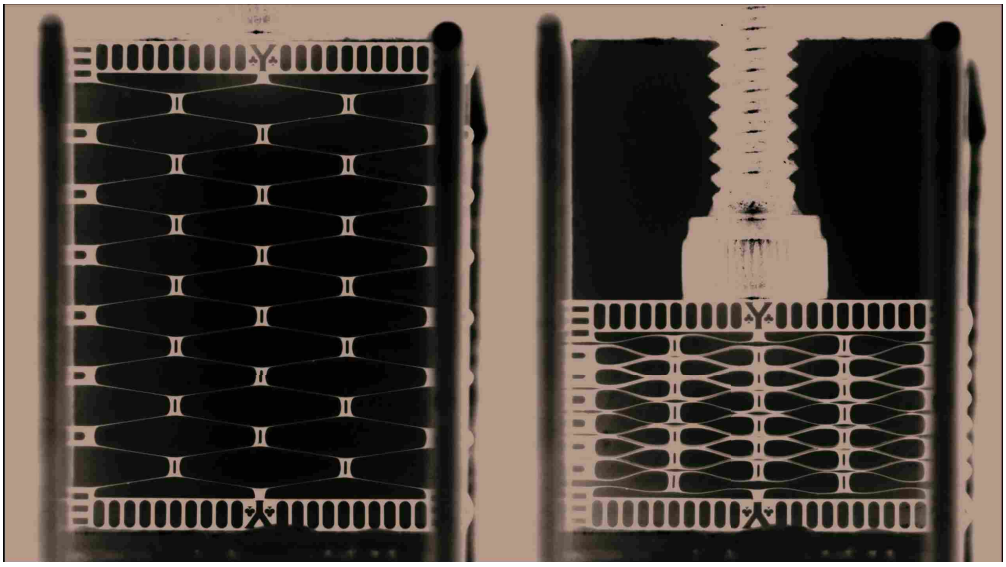

Figure 3.13: Example of CI-CNT stent mesh before and after compression

program into a spreadsheet. Initial, unstretched frames and frame-before-fracture images from the camera were saved for visual evaluation and test videos of each sample were compiled.

3.4 Results

3.4.1 Data Analysis

As with the testing performed for Chapter 2, the purpose of this effort was to demonstrate the ability of CI-CNTs to flex and deflect as would be necessary for stent compression and to specifically validate the semi-auxetic planar stent designs. These tests would also provide further validation of the material properties as noted in [21]. Because the complex mesh geometry being tested was not a simple, constant cross-section beam, we could not use the Instron force data to directly find a modulus of elasticity of the material, the strain, or the ultimate strength. Instead, a model was created in ANSYS to simulate each test independently of one another for each semi-auxetic stent designs. Figure 3.13 shows a typical test sample at the start and end of the test.

Rather than modeling a single cell from each design as done in Chapter 2, we constructed the entire array of repeated cells in the ANSYS simulation environment. Using PLANE183 elements, we created planar geometries with a constant thickness based on each sample's measured

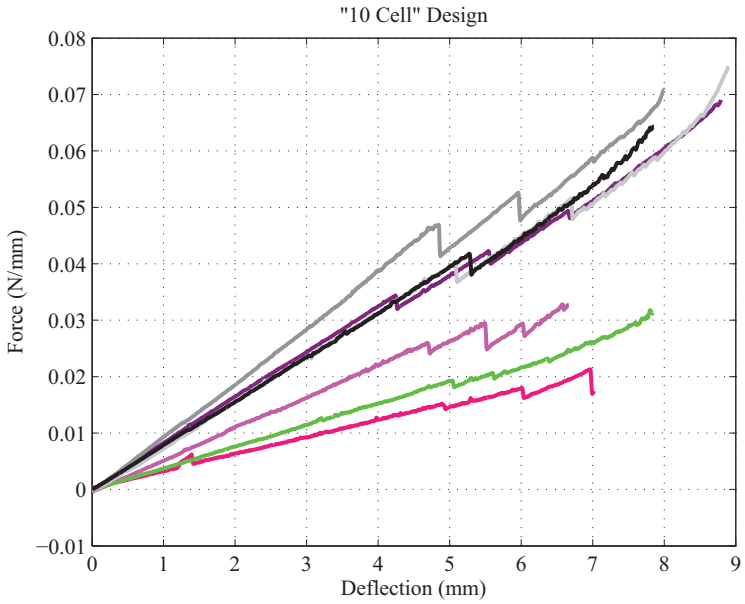

Figure 3.14: Force deflection plot of 10 Cell samples

thickness. One end of the model was fixed while the other was allowed to compress according to the data captured during testing.

We only tested complete, unbroken samples of the semi-auxetic designs, and could therefore use the force and displacement data directly from the Instron for the ANSYS analysis. We applied these data to the model in ANSYS for each test. Specifically, we used the maximum measured force and displacement at a buckle or fracture point from the Instron which then became the target for the ANSYS simulation. For each test, an initial guess for Young's Modulus was given and ANSYS was allowed to iteratively solve the simulation, changing the Young's Modulus until the resulting reaction force for a given displacement matched that which was measured with the Instron. Strain, stress, and percent elongation values at the fracture/buckle point were also obtained from this analysis.

Even after the samples reached their buckling or initial fracture point (seen as the sharp jogs in Figures 3.14 and 3.16), much of the sample was still intact and continued deflecting at approximately the same rate. We compressed the samples until they catastrophically failed, or the beams made contact with each other, and performed additional analyses in ANSYS based on these data. Specifically, we used only the maximum deflection point from end of test and the modulus from the break/buckle point analysis to calculate stress and strain. Each sample's initial

Table 3.5: Failure Modes for Each Sample

Test/ Sample ##	Failure Mode	Test/ Sample ##	Failure Mode
1	Buckle	9	Buckle
2	Break	10	Buckle
3	Break	11	Buckle
4	Buckle	12	Buckle
5	Break	13	Buckle
6	Break	14	Buckle
7	Break	15	Buckle
8	Buckle		

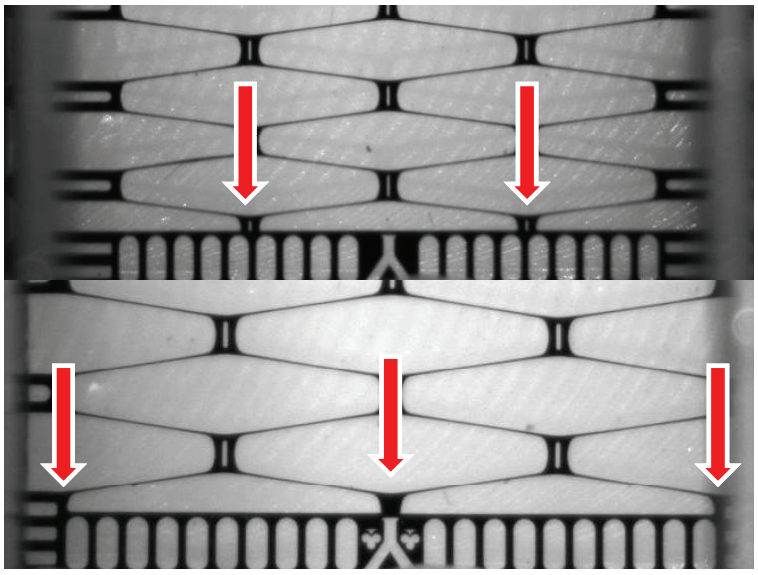

Figure 3.15: Boundary Conditions for “10 Cell” (upper) and “10 Cell V2” (lower)

failure mode is shown in Table 3.5. Percent compression values were calculated for the target 10 or 12 cell central area of the mesh (denoted by “T.A.” in the figures). Rather than attempting to match the buckling behavior seen by the samples in ANSYS, we adjusted the models and removed the lateral constraint portion of the boundary conditions which allowed the model to reach the higher compression without having to incorporate buckling. This made the model less stiff, by the factors listed in Table 3.6. Using these factors, we could correct the stress, strain, and percent compression values accordingly. Note that the “10 Cell V2” entry in the table is for two samples whose boundaries were different as shown in Figure 3.15. These two samples were fixed at three points at each end, rather than the normal two, which increased the relative stiffness.

Table 3.6: Stiffness Factors of Laterally Constrained and Unconstrained Models

10 Cell	12 Cell	10 Cell V2
1.075	1.034	1.1481

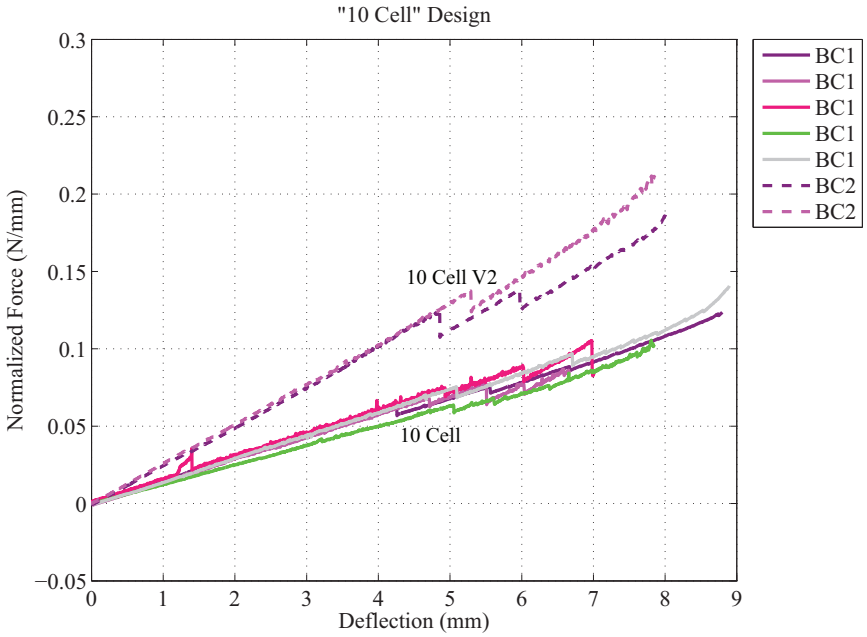

Figure 3.16: Force deflection plot of 10 Cell samples normalized by sample thickness

3.4.2 Discussion

Figure 3.14 shows the force-deflection curves for the 10 Cell design. The plot reveals that the curve, apart from the sharp points, is nearly linear and additionally, samples do not exhibit plastic deformation before failure. This translates to a linear stress-strain relation for the material up to failure. In an effort to validate the test results, we normalized the plots based on the thickness of each sample and replotted the curves. This is shown in Figure 3.16. Similar plots for the 12 Cell design can be found in Appendix B.1. We anticipated that the normalized curves for each sample should all have approximately the same slope. As can be seen in Figure 3.16, all but the two "BC2" curves match faily well. These curves correspond with the two samples which had a different boundary condition as shown previously in Figure 3.15, therefore making the sample stiffer, as represented by a steeper slope in Figure 3.16.

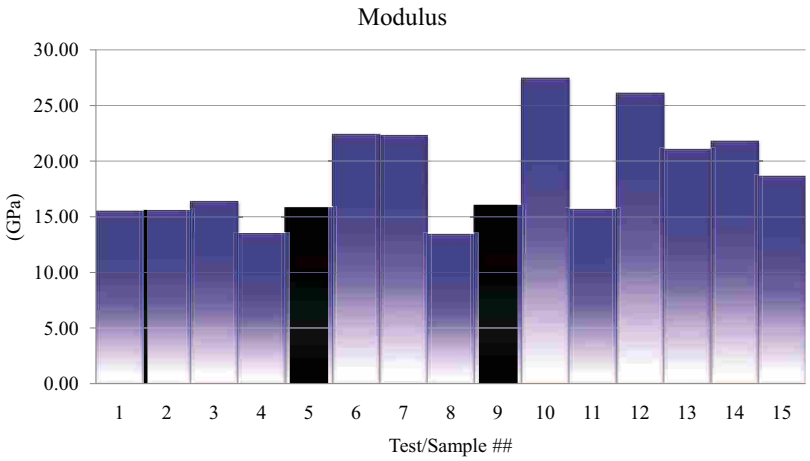

Figure 3.17: Modulus calculation of each sample tested

Figures 3.17, 3.18, and 3.19 show the simulation calculated values of Young's Modulus, maximum stress, and strain for each sample tested. Figure 3.20 shows the percent compression for tested and analyzed sample. Note the differentiation between "Break/buckle" testing point values and "End of Test" testing point values in the figures. For stents, which rely heavily on the compliance of the material to function properly, a high maximum strain is desirable. High strains translate to greater deflection before failure. The highest average strain measured in this stent pattern experiment was greater than 1% while the lowest average strain value measured was 0.62%. Modulus calculations had a similar range of values. The highest average modulus calculated was close to 27 GPa while the lowest was close to 13 GPa. Percent elongation at buckle/break reached a maximum of 47% with all samples surpassing 20%. Percent elongation at the end of test reached a maximum of 62% with all samples surpassing 44%.

Even though the semi-auxetic designs performed largely as anticipated, we can see variability in the results. After conducting the experiments, we feel there were some major factors contributing to the variation. First, these tests were completed over a relatively long period of time so that they are affected by process variation over time. More specifically, each machine or piece of equipment used was likely affected by other experiments or work using the same machine. Additionally, these samples behaved like typical ceramics or any material with brittle failure characteristics. That is, it is difficult to control ceramic materials on the grain level where weaknesses and imperfections occur. This typically leads to earlier than anticipated fracture. We hypothesize that this is why some of the tested samples break before the laterally constrained end cells of the

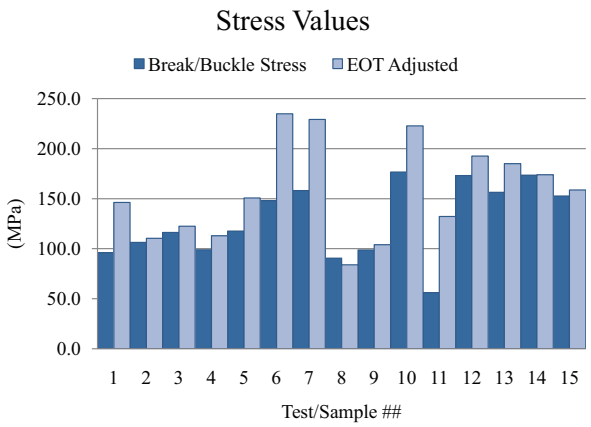

Figure 3.18: Stress calculation of each sample tested

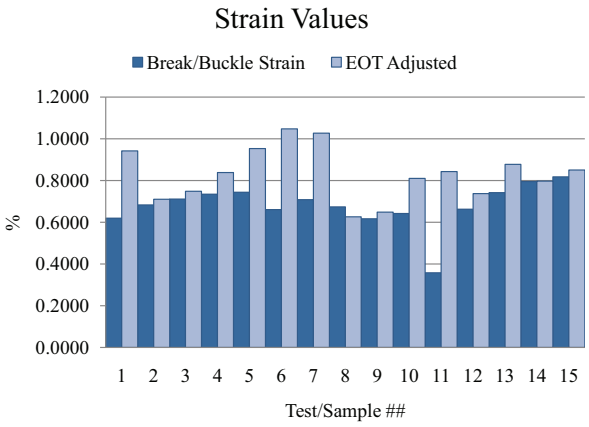

Figure 3.19: Strain calculation of each sample tested

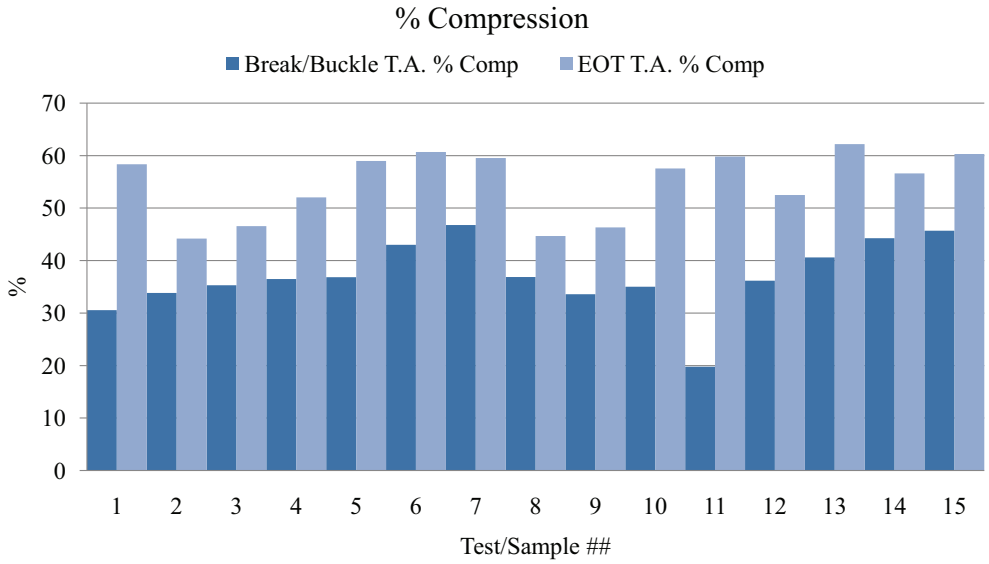

Figure 3.20: Bar graph showing the percent compression for each sample

same sample buckle during compression. In testing full, unbroken samples of the semi-auxetic designs, we significantly increased the possibility that such an imperfection existed at any one of the many critical geometry locations. These are the most complex designs that have been made using this process. It is therefore expected to find areas where improvements could be made.

The calculated values for Young's Modulus in this data set are no lower than 13 GPa and reach as high as 26 GPa. In constrast, samples tested in Chapter 2 had values ranging from 5 GPa to only 14 GPa, using the same testing and data analysis methods. We hypothesize that this

difference is due to the change in infiltration geometry. Specifically, the structures in Chapter 2 were larger than those in this chapter, which likely decreased the infiltration density of the CI-CNT material. We also saw this effect with the relatively large compression samples analyzed in Chapter 2, showing infiltration void evidence with SEM imagining in Figure 2.14. Further, modulus values noted in [21] for structures larger than those tested in this chapter were between 4 GPa and 15 GPa. It would be useful to study and quantify the effect of size on infiltration density, and subsequently CI-CNT modulus.

3.4.3 Cylindrical Finite Element Analysis

As mentioned previously, the fabrication process, including machines and equipment, was not configured for cylindrical fabrication in this work. However, these semi-auxetic designs were implemented into finite element models of the same design in a cylindrical configuration. Figures 3.21 and 3.22 show images of the simulated cylindrical semi-auxetic 12 Cell stent design having undergone full 66% compression (3 mm to 1 mm). Similar plots for the 10 Cell design can be found in Appendix C.2.

The modeling is valuable because it shows what kind of stress and strain can be anticipated for a given displacement. Table 3.7 shows different stress and strain values taken from ANSYS simulations at the maximum and minimum modulus values as shown in section 3.4.2. Between the two extremes, we can assume that there is a linear relation. It is important to note that these values are for a radial thickness of 150 μm and as the model compressed radially, stresses are not evenly distributed throughout the material's thickness. While the planar geometry only experienced tension and compression throughout the geometry thickness, the cylindrical model shows the radial motion induces more complex, unevenly distributed stress. The values in Table 3.7, based on the testing results of this chapter, show that the semi-auxetic designs can function in a stent application. Lastly, this modeling is useful as it was discovered that cylindrical modeling and compression in ANSYS is not trivial, and could be a starting point for further investigation.

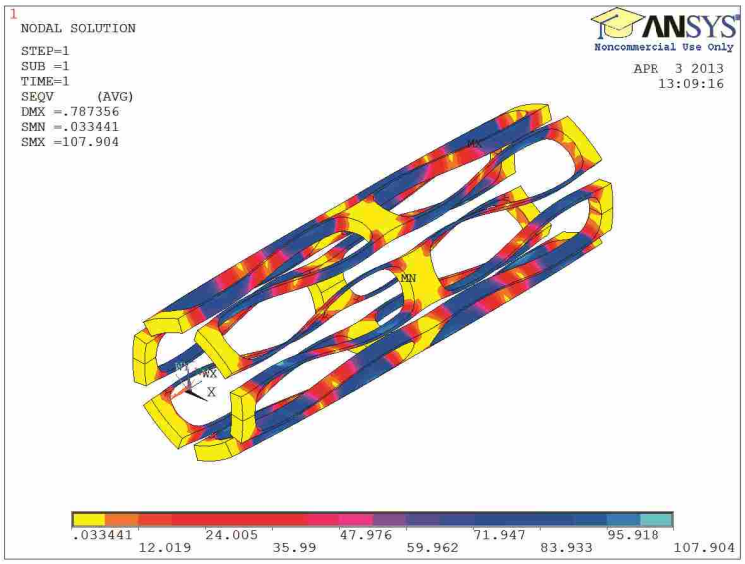

Figure 3.21: ANSYS finite element model of 12 Cell design applied in a cylindrical configuration showing maximum stress values

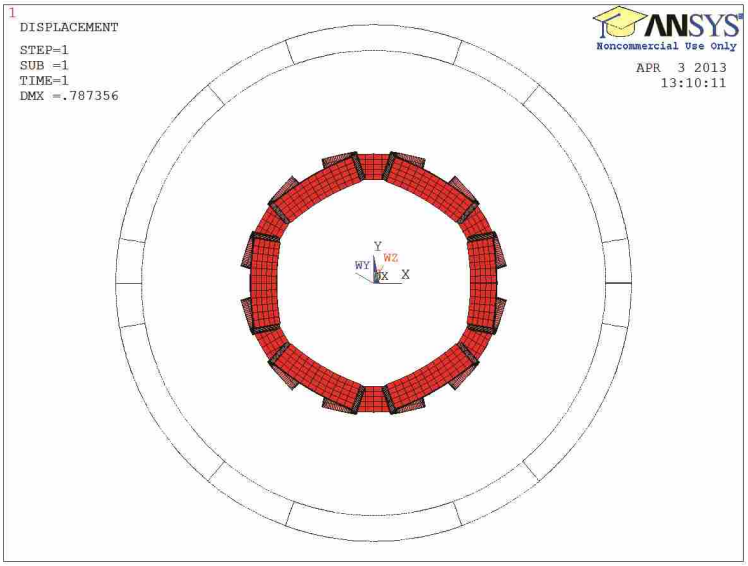

Figure 3.22: ANSYS finite element model of 12 Cell design applied in a cylindrical configuration showing 3mm to 1mm diameter compression

3.5 Conclusions and Recommendations

We conducted an experiment to validate the potential capabilities of the CNT-M process to create planar semi-auxetic stent geometries of the same shape and size as stents currently on the maket. Once the structures were fabricated, they were tested in compression to demonstrate the

Table 3.7: Cylindrical FEA Stent Simulations (150μm thick)

	Modulus (GPa)	Max Stress (MPa)	Max Strain (%)
10 Cell	13	115.7	0.9
10 Cell	27	240.35	0.9
12 Cell	13	107.9	0.83
12 Cell	27	224.1	0.83

material's flexibility and measure strain values. In addition to the measurement of strain values, Young's modulus was also measured/calculated to confirm the material as pyrolytic carbon. Next, the percent elongation of individual cells was measured. We found that stent-like structures composed of pyrolitic carbon, as fabricated using the CNT-M process, can deflect sufficiently, without fracturing and could therefore potentially be used in stent applications. We also note how the structures are succeptible to variabiliy in the CNT-M fabrication process. Lastly, we performed a finite element model simulation of the semi-auxetic designs in a cylindrical configuration which showed the expectations for stress and strain in a 66% compression application. These stress and strain values are in the usable range of the CI-CNT material.

CHAPTER 4. CONCLUSIONS AND RECOMMENDATIONS

4.1 Summary of Contributions

This thesis contributes useful knowledge regarding the possibility of fabricating arterial stents from CI-CNT material. The major areas of contributions in this thesis are: additional material property characterization data for CI-CNTs, the modification of the CI-CNT fabrication process as tailored to stent-like geometries, the modification of CI-CNT designs to be better suited for the fabrication process, the design and optimization of two similar semi-auxetic stent geometries, and the testing and demonstration of these geometries in stent-like compression applications.

4.1.1 Material Property Data Collection

One of the major areas where this work contributes meaningful research is regarding the material properties of the CI-CNT material. Characterization of pyrolitic carbon properties is already found in the literature, but little can be found about pyrolitic carbon specifically made using the CI-CNT process discussed in this thesis. To add to the global understanding of this material, tensile and compression tests were both performed on CI-CNT samples of different geometries and relative sizes to find the ulimate strength in both directions, as well as strain and Young's modulus expectations. The effect of carbon infiltration on larger vs smaller geometries was investigated. To the extent laboratories and equipment facilitated, the repeatablility of producing CI-CNT with consistent mechanical properties was also explored. We suggested that the modulus may depend on design geometry, where smaller or thinner structures allowed for better infiltration and therefore a higher modulus. The samples in this work were found to have moduli ranging from 5 to 27 GPa, with the majority being between 10 and 20 GPa. We also found fracture strength greater than 100 MPa, with it sometimes getting as high as 200 MPa. Lastly, fracture strain values were measured, with the maximum reaching 1.4% and the average between 0.75-1%.

4.1.2 Design and Optimization of Two Semi-Auxetic Stent Geometries

This work has successfully demonstrated the ability of CI-CNT pyrolitic carbon to function in an artertial stent application. Two different, yet similar semi-auxetic stent geometries were designed and optimized to distribute loads along the flexible segments of the ceramic CI-CNT material. For the specific design requirements of an arterial stent, namely the expanded and compressed diameters, we concluded that the semi-auxetic designs are able to expand and compress while staying within the usable material constraints as dictated by CI-CNT's mechanical properties. Additionally, these designs were applied in a cylindrical configuration finite element analysis model, which likewise demonstrates the designs' functionality within the material's property constraints.

4.1.3 Testing of Geometries in Stent-like Applications

Perhaps most importantly, this work has presented the testing results of these stent geometries, specifically targeting the necessary expansion and compression requirements for arterial stent applications. These tests have demonstrated the ability of the CI-CNT material to be designed and fabricated into geometries that can handle stent application compressions and expansions. These tests have also revealed some potential weaknesses of the material's ceramic nature, and the possible variability associated with CI-CNT fabrication. The ceramic nature of the CI-CNTs lends itself to fracture at weak locations (if present) before the anticipated fracture strength has been reached. Additionally, we have concluded that a tightly controlled process (including fabrication machines) environment is necessary to ensure consistent results and a CI-CNT material whose imperfections have been minimized.

4.1.4 Modification of the CI-CNT Fabrication Process

The CI-CNT fabrication process was not developed in this work; however, the process was successfully modified to better handle the fabrication of stent-like geometries. This included parameter adjustment on some of the individual fabrication machines as well as the addition of some etching processes specifically designed to separate the delicate stent geometries from wafer substrates. Previous work perfomed with the CI-CNT material relied heavily on the intrinsic stresses

after infiltration to "curl" and separate the CI-CNT structure from the substrate. The additions of plasma etching and KOH etching used in this thesis provides additional separation methods for complex geometry and geometry sensitive to curling.

4.1.5 Design Considerations for the CI-CNT Fabrication Process

In addition to the CI-CNT fabrication process itself being modified, the designs to be fabricated were also made to be more fabrication friendly. In other words, once a model or design to fabricate has been chosen, certain adjustments and additions to the design have to be made. These adjustments and additions do not affect the design's intended funtionality or geometric specifications, but rather the ease of fabrication. In this work, we made support structures smaller than the stent structure and designed them to be simple squares. This allowed the support structures to promote CNT growth height and straightness during growth and infiltration. This also allowed us to remove the stent structures without them getting caught in the support structures. We also placed "holes" in the sections of geometry which contained a large surface area. These holes minimized cracking after infiltration and allowed for the sample's release from the substrate by plasma etching alone instead of KOH etching.

4.2 Recommendations

The work presented in this thesis contributes to the overall data and understanding of CI-CNT production using microfabrication techniques as a potential arterial stent material. In performing this research, however, additional avenues of further investigation were discovered which provide opportunities to more completely explore related ideas including cylindrical configurations, CI-CNT composites, and biocompatibility.

4.2.1 Cylindrical Configuration

As is well known, a stent is tubular or cylindrical in shape. Rather than focusing on the setup, conguration, and hardware associated with the fabrication of cylindrical stents using microfabrication processes, this work focused on the design and fabrication of stent patterns in a planar configuration as a precursor to cylindrical fabrication. The testing, analysis, and results in this

work lays the foundation for cylindrical stent design as the modified fabrication process targeted toward tubular samples is developed. This development could include such process modifications and hardware alterations required to perform curved surface photolithograhy and mask creation, carefully controlled thermal evaporation of iron and aluminum onto a cylindrical, rotating surface, and the release of a CI-CNT structure from a cylindrical substrate or mandrel.

In addition to the development of cylindrical fabrication processes, the testing of such devices will also likely need to be considered. It is relatively straightforward to concieve of testing methods and approaches for planar stent designs, but cylindrical sample testing may prove to be more interesting. Potential tests could include radial stiffness and deflection testing as well as lateral bending tests, while the stent is compressed, to simulate stent delivery from the femoral artery to the affected arterial location.

4.2.2 CI-CNT Composites

While this work only focused on pure CI-CNT material, it is not only possible, but very feasible and almost certainly advantageous to combine the CI-CNT material with other materials. As mentioned above, the CNTs only account for a fraction of a percent of the entire solid structure volume. The rest of the volume is produced by infiltrating the empty space between individual CNTs with, in this case, amorphous carbon. This space, however, could potentially be filled with other materials in an effort to increase the usability or advantages of the CNT-filled material.

There is a myriad of potentially advantageous materials to be used in this application. For example, the CNTs could be partially infiltrated with carbon as usual, for the purpose of holding the CNT structure together, and the remaining space could be filled with a drug eluting polymer. This type of system would differ from current drug eluting stents in that the drug is not a coating around a bare metal stent, but rather part of the stent itself. As the the polymeric drug breaks down into the body, what remains is a biocompatible, pyrolitic carbon stent.

In addition to the possibiliy of infiltrating the CNTs with a drug eluting polymer, materials could be infiltrated for the purpose of adjusting and optimizing material properties. This work, as well as other publications, has sought to characterize the material properties of the pure CI-CNT material. Various combinations of polymers, whether infiltrated or otherwise deposited in the CNT forest, open a vast range of possible material properties for the composite stent. This could prove to

be advantageous in optimizing stent materials specifically for the dynamics of stent expansion and compression. Further, because no two blood vessels are identical, designing a stent with custom material properties for a specific patient could prove to decrease some problems associated with stent implantation. For example, each stent could be designed with a specific stiffness based on the mechanical properties of the artery in a particular patient. Beyond the material's mechanical properties, chemical and biological response properties for a particular patient could be analyzed and used to produce individual stent materials based on the patient in which they would be inserted.

4.2.3 Biocompatibility

As discussed in Chapter 1, the biocompatibility of any foreign object that is inserted into the body is of utmost importance. The biocompatibility of an arterial stent is likely of even greater importance. While there is a large amount of data and results in the literature regarding the biocompatibility of CNTs and carbon filled CNTs, further work to quantify the biocompatibility of carbon filled CNT stents and stent designs created with microfabrication techniques could be pursued. As the production of carbon filled CNT stents using microfabrication processes is relatively new and unexplored, the material's chemical structure could differ from that of other similar materials created using different methods of fabrication and therefore potentially produce different results.

In addition to a material's chemical composition and crystalline structure, biocompatibility is often closely associated with the surface condition of the material. This is especially true in vessels where fluid flows. Blood vessels, for example, contain platelets which act as a defense mechanism and clot to protect the body. If an implanted device, whether it be an arterial stent or not, could be rejected by the body not because the material itself is not compatible with the body, but because the device's surface was poorly processed. The "rough" surface increases the possibility that platelets would collect on the device's edges, reduce flow area in the region, and possibly become a thombotic danger to the patient. Figure 4.1 shows a typical surface composition of this work's CI-CNT process.

To address this issue, measurements of surface roughness could be taken on the top and sides of the CI-CNT structure. With current silicon wafer fabrication methods, the bottom surface roughness is already as low as the wafer itself, which is typically on the order of nanometers. Post processing methods to smooth the surfaces could be investigated as to their effectiveness and

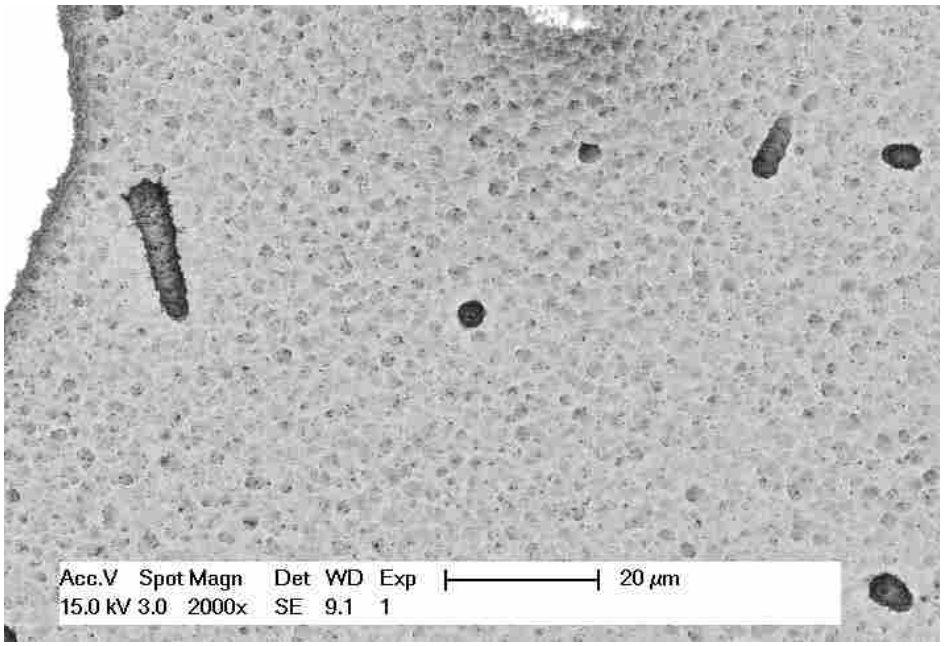

Figure 4.1: SEM image showin top surface of C-CNT material

plausibility in the CI-CNT stent fabrication process. Standard post processing methods including grinding and polishing would likely be extremely difficult and labor intensive on the relatively delicate stent structure while microfabrication processes such as oxidation and etching could potentially reduce surface roughness.

REFERENCES

[1] Hoyert, D. L., 2012. "75 years of mortality in the united states, 1935-2010." *NCHS Data Brief,* **88**.

[2] Hoyert, D. L., and Xu, J., 2012. "Deaths: Preliminary data for 2011." *National Vital Statistics Reports,* **61,6**.

[3] Gutman, D., and Golomb, G., 2012. "Liposomal alendronate for the treatment of restenosis." *Journal of Controlled Release,* **161**, pp. 619–627.

[4] Hopkins, J., McLaughlin, C. W., Johnson, S., Warner, M. Q., LaHart, D., and Wright, J. D., 1993. *Human Biology and Health*. Prentice Hall.

[5] Gaziano, J., Ridker, O., and Libby, P., 2011. *Braunwald's Heart Disease: A Textbook of Cardiovascular Medicine*. Saunders Elsevier.

[6] National Institutes of Health, 2012. What is coronary heart disease? Website http://www.nhlbi.nih.gov.

[7] Nguyen, T., Hung, P. M., Tuan, N. Q., Hermiller, J., Douglas, J. S., and Grines, C., 2001. "Balloon angioplasty." *Journal of Interventional Cardiology,* **14(5)**, pp. 563–569.

[8] Hansi, C., Arab, A., Rzany, A., Ahrens, I., Bode, C., and Hehrlein, C., 2009. "Differences of platelet adhesion and thrombus activation on amorphous silicon carbide, magnesium alloy, stainless steel, and cobalt chromium stent surfaces." *Catheterization and Cardiovascular Interventions,* **73**, pp. 488–496.

[9] National Institutes of Health, 2012. How are stents placed? Website http://www.nhlbi.nih.gov/.

[10] Serruys, P., Luijten, H., Beatt, K., Geuskens, R., de Feyter, P., van den Brand, M., Reiber, J., ten Katen, H., van Es, G., and Hugenholtz, P., 1988. "Incidence of restenosis after successful coronary angioplasty: a time-related phenomenon. a quantitave angiographic study in 342 consecutive patients at 1, 2, 3, and 4 months." *Journal of the American Heart Association,* **77**, pp. 361–371.

[11] Iakovou, I., Schmidt, T., Bonizzoni, E., Ge, L., Sangiorgi, G. M., Stankovic, G., Airoldi, F., Chieffo, A., Montorfano, M., Carlino, M., Michev, I., Corvaja, N., Briguori, C., Gerckens, U., Grube, E., and Colombo, A., 2005. "Incidence, predictors, and outcome of thrombosis after successful implantation of drug-eluting stents." *Journal of the American Medical Association,* **293**(17), pp. 2126–2130.

[12] Morice, M.-C., Serruys, P. W., Sousa, J. E., Fajadet, J., Ban Hayashi, E., Perin, M., Colombo, A., Schuler, G., Barragan, P., Guagliumi, G., Molnar, F., and Falotico, R., 2002. "A randomized comparison of a sirolimus-eluting stent with a standard stent for coronary revascularization." *New England Journal of Medicine,* **346**(23), pp. 1773–1780.

[13] Moses, J. W., Leon, M. B., Popma, J. J., Fitzgerald, P. J., Holmes, D. R., O'Shaughnessy, C., Caputo, R. P., Kereiakes, D. J., Williams, D. O., Teirstein, P. S., Jaeger, J. L., and Kuntz, R. E., 2003. "Sirolimus-eluting stents versus standard stents in patients with stenosis in a native coronary artery." *New England Journal of Medicine,* **349**(14), pp. 1315–1323.

[14] VanderLaan, P. A., Padera, R. F., and Schoen, F. J., 2012. "Practical approach to the evaluation of prosthetic mechanical and tissue replacement heart valves." *Current Concepts in Cardiovascular Pathology,* **5**, pp. 353–369.

[15] Stary, V., Bacakova, L., Hornik, J., and Chmelik, V., 2003. "Bio-compatibility of the surface layer of pyrolytic graphite." *Thin Solid Films,* **433**, pp. 191 – 198.

[16] Ratner, B. D., Hoffman, A. S., Shoen, F. J., and Lemons, J. E., 2004. *Biomaterials Science: An Introduction to Materials in Medicine*. Elsevier Academic Press.

[17] Antoniucci, D., Bartorelli, A., Valenti, R., Montorsi, P., Santor, G. M., Fabbiocchi, F., Bolognese, L., Loaldi, A., Trapani, M., Trabattoni, D., Moschi, G., and Galli, S., 2000. "Clinical and angiographic outcome after coronary arterial stenting with the carbostent." *The American Journal of Cardiology,* **85**, pp. 821–825.

[18] Cook, S. D., Beckenbaugh, R. D., Redondo, J., Popich, L. S., Klawitter, J. J., and Linscheid, R. L., 1999. "Long term follow-up of pyrolytic carbon metacarpophalangeal inplants." *The Journal of Bone and Joint Surgery,* **81**, pp. 635–648.

[19] Hutchison, D. N., Morrill, N. B., Aten, Q., Turner, B. W., Jensen, B. D., Howell, L. L., Vanfleet, R. R., and Davis, R. C., 2010. "Carbon nanotubes as a framework for high-aspect-ratio MEMS fabrication." *Journal of Microelectromechanical Systems,* **19**, pp. 75–82.

[20] Moulton, K., 2010. "Straightness of growth for carbon nanotube microelectromechanical systems." Master's thesis, Brigham Young University.

[21] Fazio, W. C., Lund, J. M., Wood, T. S., Jensen, B. D., Davis, R. C., and Vanfleet, R. R., 2011. "Material properties of carbon-infiltrated carbon nanotube-templated structures for microfabrication of compliant mechanisms." In *Proceedings of the ASME 2011 Internaltional Mechanical Engineering Congress & Exposition*, no. 64168.

[22] Huang, Y., Venkatraman, S. S., Boey, F. Y., Lahti, E. M., Umashankar, P., Mohanty, M., Arumugam, S., Khanolkar, L., and Vaishnav, S., 2010. "In vitro and in vivo performance of a dual drug-eluting stent (ddes)." *Biomaterials,* **31**, pp. 4382–4391.

[23] Schmidt, W., Lanzer, P., Behrens, P., Topoleski, L., and Schmitz, K.-P., 2009. "A comparison of the mechanical performance characteristics of seven drug-eluting stent systems." *Catheterization and Cardiovascular Interventions,* **73**, pp. 350–360.

[24] Howell, Larry, L., 2001. *Compliant Mechanisms*. Wiley Interscience.

[25] Serruys, P., Kutrykm, M., and Ong, A., 2006. "Coronary-artery stents." *The New England Journal of Medicine,* **354**, pp. 483–495.

[26] Pesakova, V., Klezl, Z., Balik, M., and Adam, M., 2000. "Biomechanical and biological properties of the implant material carbon-carbon composite covered with pyrolytic carbon." *Journal of Materials Science: Materials in Medicine,* **11**, pp. 793–798.

[27] Auricchio, F., Di Loreto, M., and Sacco, E., 2001. "Finite-element analysis of a stenotic artery revascularization through a stent insertion." *Computer Methods in,* **4**, pp. 249–263.

[28] Migliavacca, F., Petrini, L., Colombo, M., Auricchio, F., and Pietrabissa, R., 2002. "Mechanical behavior of coronary stents investigated through the finite element method." *Journal of Biomechanics,* **35**, pp. 803–811.

[29] Gaspar, N., Ren, X., Smith, C., Grima, J., and Evans, K., 2005. "Novel honeycombs with auxetic behavior." *Acta Materialia,* **53**, pp. 2439–2445.

[30] Grima, J. N., Farrugia, P. S., Caruana, C., Gatt, R., and Attard, D., 2008. "Auxetic behavior from stretching connected squares." *The Journal of Material Science,* **43**, pp. 5962–5971.

[31] Prawoto, Y., 2012. "Seeing auxetic materials from the mechanics point of view: A structural review on the negative poisson's ratio." *Computational Materials Science,* **58**, pp. 140–153.

APPENDIX A. ADDITIONAL TABLES

A.1 Optimized Taper Stress at Max Deflection

Table A.1: Optimized Taper Stress at Max Deflection (8 Cell)(MPa)

		Beam Width (μm)					
		25	23	21	19	17	15
Half Cell Width (mm)	1.5	387.13	355.2	347.10	335.69	324.29	296.7
	1.75	272.53	263.10	251.32	239.93	219.89	210.67
	2	208.94	195.99	186.15	182.63	170.73	165.35
	2.25	160.31	152.84	144.01	135.15	127.31	116.06
	2.5	127.9	121.44	115.03	109.05	100.7	95.58

Table A.2: Optimized Taper Stress at Max Deflection (12 Cell)(MPa)

		Beam Width (μm)					
		25	23	21	19	17	15
Half Cell Width (mm)	1.5	228.3	220.8	206.47	196.7	189.00	171.82
	1.75	158.83	155.54	146.47	139.83	128.44	121.09
	2	122.61	116.21	109.7	103.26	96.34	89.5
	2.25	95.16	89.95	83.93	78.77	74.21	67.64
	2.5	75.68	71.4	66.50	62.67	58.74	54.24

A.2 Optimized Taper Reaction Force/Stress Ratio

Table A.3: Optimized Taper Reaction Force/Stress Ratio (8 Cell)(Units Arbitrary)

		Beam Width (μm)					
		25	23	21	19	17	15
Half Cell Width (mm)	1.5	High Str	High Str	High Str	High Str	High Str	High Str
	1.75	High Str	High Str	High Str	High Str	High Str	High Str
	2	High Str	High Str	High Str	High Str	High Str	High Str
	2.25	High Str	High Str	High Str	High Str	0.4716	0.3967
	2.5	0.5858	0.5260	0.4740	0.4221	0.3568	0.3057

Table A.4: Optimized Taper Reaction Force/Stress Ratio (12 Cell)(Units Arbitrary)

		Beam Width (μm)					
		25	23	21	19	17	15
Half Cell Width (mm)	1.5	High Str	High Str	High Str	High Str	High Str	High Str
	1.75	High Str	High Str	High Str	High Str	0.4898	0.4447
	2	0.5673	0.5120	0.4617	0.4341	0.3674	0.3246
	2.25	0.4359	0.4001	0.3672	0.3316	0.2949	0.2537
	2.5	0.3690	0.3476	0.3056	0.2737	0.2420	0.2008

A.3 Sample Testing Data

Table A.5: Chapter 2 Testing Data up to failure

Sample	Modulus (Gpa)			Strain (%)			Stress (Mpa)			% Elong.
	Ave	Min	Max	Ave	Min	Max	Ave	Min	Max	
1	14.622	15.945	13.311	0.659	0.640	0.679	96.29	102.00	90.39	79.104
2	11.405	13.759	9.441	0.699	0.646	0.745	79.76	88.83	70.29	81.141
3	12.457	13.617	11.736	1.379	1.332	1.396	171.75	181.40	163.85	143.531
4	13.986	14.942	13.028	0.983	0.947	1.006	137.54	141.52	131.11	96.209
5	9.081	11.024	7.461	0.420	0.399	0.449	38.13	43.99	33.51	45.793
6	6.540	8.472	5.213	0.496	0.437	0.523	32.44	37.01	27.28	64.793
7	6.909	7.971	6.144	0.626	0.593	0.653	43.28	47.29	40.14	59.439
8	5.637	7.594	4.807	1.449	1.196	1.449	81.70	90.81	69.67	117.169
9	10.012	11.753	9.670	0.636	0.602	0.647	63.64	70.75	62.56	73.737
10	4.604	5.584	3.580	0.697	0.642	0.744	32.11	35.85	26.63	74.112
11	6.042	8.032	5.080	1.428	1.274	1.536	86.28	102.31	78.04	113.509

Table A.6: Chapter 3 Testing Data up to Break/Buckle

Sample Info					Up to Break/Buckle						
Sample ID	Design	Thick (mm)	Total Flex Height (mm)	T.A. Height (mm)	Max σ (Mpa)	Max ε (%)	Calc. E (Gpa)	Max F (N)	Max δ (mm)	T.A. Disp (mm)	T.A. % Comp
T4ID11	10 Cell	0.559	15.080	9.425	96.039	0.619	15.511	0.034	4.240	2.879	30.550
T5ID15	10 Cell	0.381	15.080	9.425	106.264	0.683	15.556	0.026	4.686	3.189	33.831
T10ID23	10 Cell	0.203	15.080	9.425	116.289	0.711	16.358	0.015	4.884	3.326	35.289
T20ID13A	10 Cell	0.305	15.080	9.425	98.884	0.734	13.466	0.019	5.046	3.440	36.494
T21ID17A	10 Cell	0.533	15.080	9.425	117.569	0.744	15.806	0.040	5.091	3.470	36.820
T22ID20A	10 Cell V2	0.381	13.195	9.425	147.975	0.660	22.409	0.048	4.855	4.054	43.017
T23ID21A	10 Cell V2	0.305	13.195	9.425	158.046	0.709	22.302	0.042	5.291	4.409	46.780
T2DID7	12 Cell	0.432	14.137	9.425	90.499	0.674	13.422	0.026	4.600	3.473	36.850
T7ID20	12 Cell	0.229	14.137	9.425	98.754	0.617	16.007	0.015	4.196	3.165	33.579
T14ID5A	12 Cell	0.216	14.137	9.425	176.573	0.642	27.484	0.026	4.375	3.302	35.031
T15ID6A	12 Cell	0.597	14.137	9.425	56.039	0.358	15.670	0.023	2.470	1.863	19.762
T16ID7A	12 Cell	0.152	14.137	9.425	173.027	0.662	26.128	0.018	4.515	3.408	36.159
T17ID8A	12 Cell	0.546	14.137	9.425	156.380	0.742	21.062	0.058	5.060	3.828	40.613
T18ID9A	12 Cell	0.508	14.137	9.425	173.563	0.796	21.813	0.061	5.506	4.171	44.251
T19ID10A	12 Cell	0.533	14.137	9.425	152.631	0.818	18.656	0.056	5.680	4.306	45.689

Table A.7: Chapter 3 Testing Data Through End of Test

Sample Info					End of Test				
Sample ID	Design	Thick (mm)	Total Flex Height (mm)	T.A. Height (mm)	Adjusted σ (Mpa)	Adjusted ε (%)	Max δ (mm)	T.A. Disp (mm)	T.A. % Comp
T4ID11	10 Cell	0.559	15.080	9.425	146.182	0.942	8.800	5.500	58.355
T5ID15	10 Cell	0.381	15.080	9.425	110.480	0.710	6.666	4.166	44.203
T10ID23	10 Cell	0.203	15.080	9.425	122.416	0.748	7.019	4.387	46.546
T20ID13A	10 Cell	0.305	15.080	9.425	112.845	0.838	7.846	4.904	52.027
T21ID17A	10 Cell	0.533	15.080	9.425	150.629	0.953	8.896	5.560	58.990
T22ID20A	10 Cell V2	0.381	13.195	9.425	234.782	1.048	8.006	5.719	60.676
T23ID21A	10 Cell V2	0.305	13.195	9.425	229.153	1.027	7.856	5.612	59.538
T2DID7	12 Cell	0.432	14.137	9.425	83.993	0.626	6.000	4.210	44.668
T7ID20	12 Cell	0.229	14.137	9.425	103.883	0.649	6.220	4.364	46.302
T14ID5A	12 Cell	0.216	14.137	9.425	222.660	0.810	7.729	5.423	57.538
T15ID6A	12 Cell	0.597	14.137	9.425	132.139	0.843	8.036	5.638	59.822
T16ID7A	12 Cell	0.152	14.137	9.425	192.618	0.737	7.050	4.946	52.477
T17ID8A	12 Cell	0.546	14.137	9.425	184.892	0.878	8.355	5.862	62.193
T18ID9A	12 Cell	0.508	14.137	9.425	173.821	0.797	7.606	5.337	56.622
T19ID10A	12 Cell	0.533	14.137	9.425	158.605	0.850	8.100	5.683	60.295

APPENDIX B. ADDITIONAL PLOTS

B.1 Force Deflection Plots for 12 Cell design

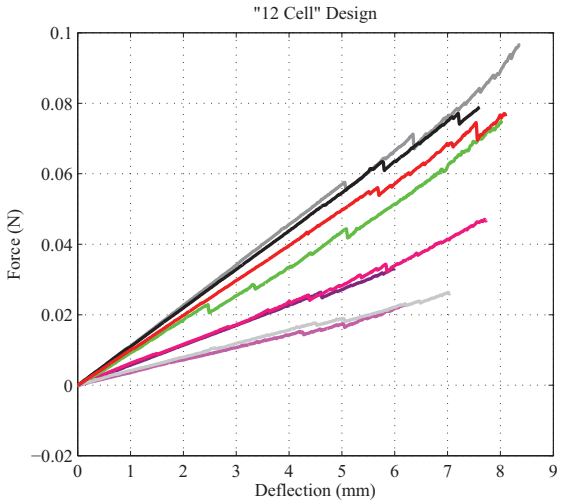

Figure B.1: Force deflection plot of 12 Cell samples

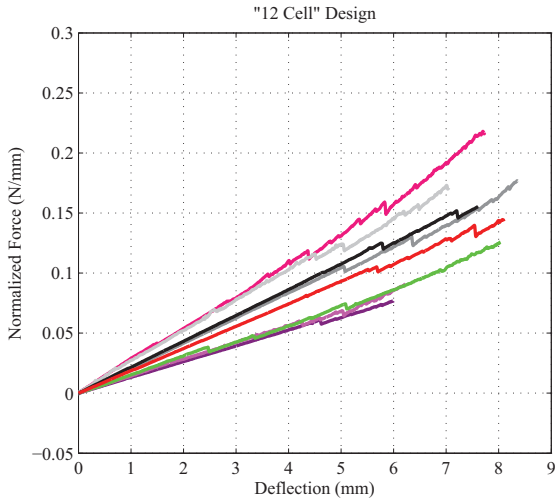

Figure B.2: Force deflection plot of 12 Cell samples normalized by sample thickness

B.2 Validation Plots for 8 and 12 Cell Spline Optimizations

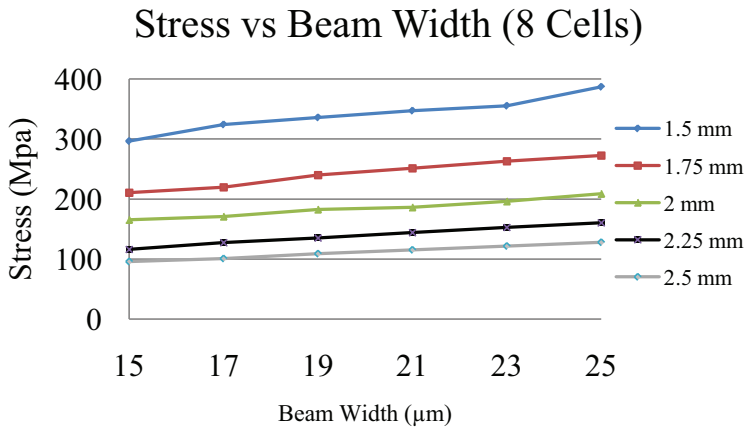

Figure B.3: Stress vs beam width of the 8 Cell spline optimization results

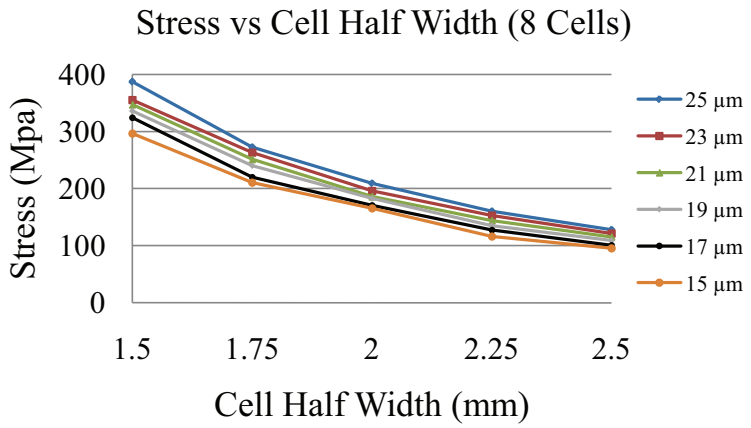

Figure B.4: Stress vs cell half width of the 8 Cell spline optimization results

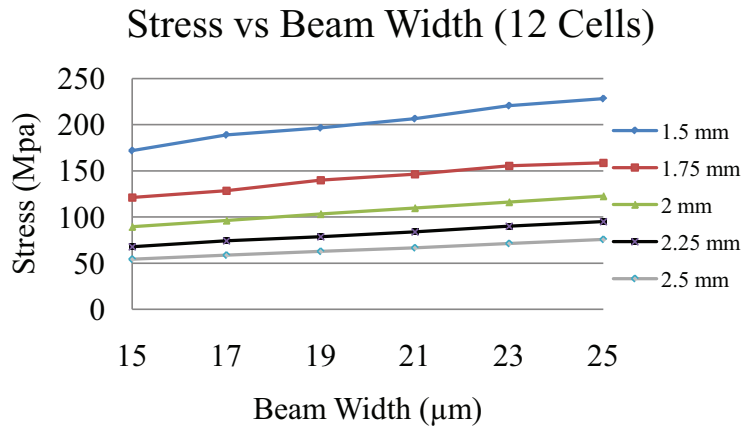

Figure B.5: Stress vs beam width of the 12 Cell spline optimization results

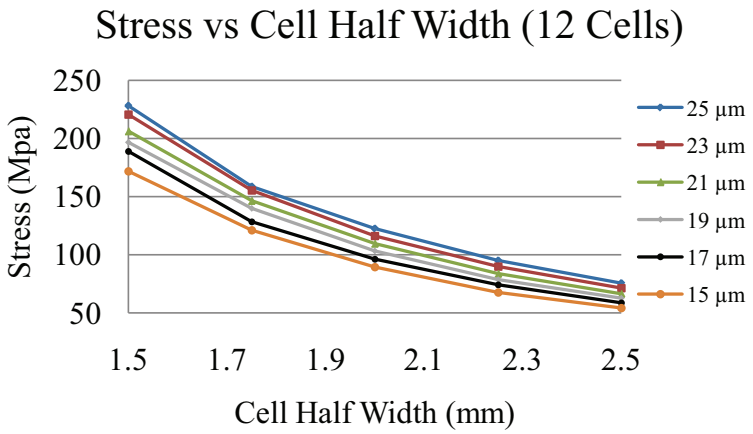

Figure B.6: Stress vs cell half width of the 12 Cell spline optimization results

APPENDIX C. DRAWINGS AND FEA IMAGES

C.1 Semi-Auxetic Design Drawings

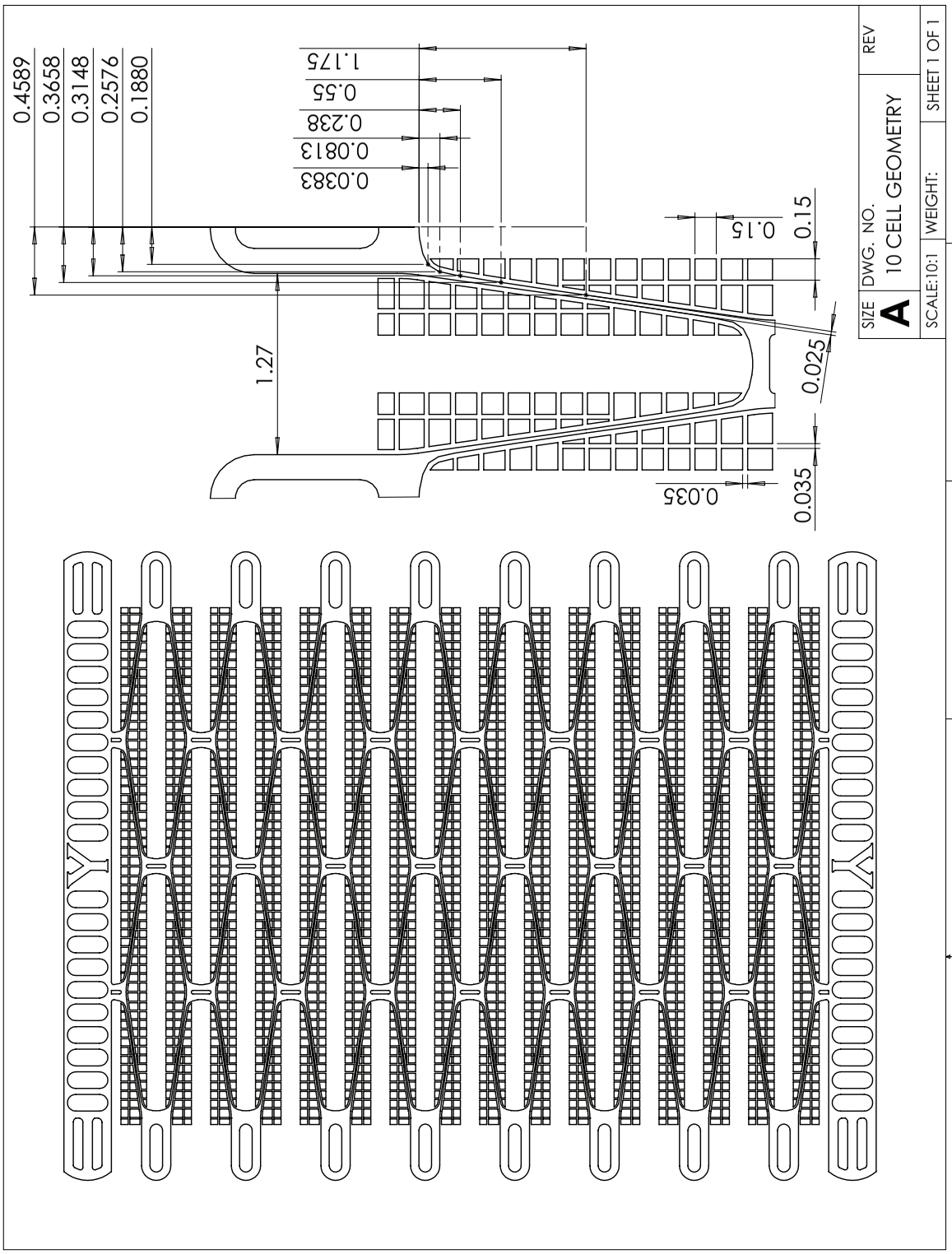

Figure C.1: Critical Planar Dimensions of 10 Cell Semi-Auxetic Design

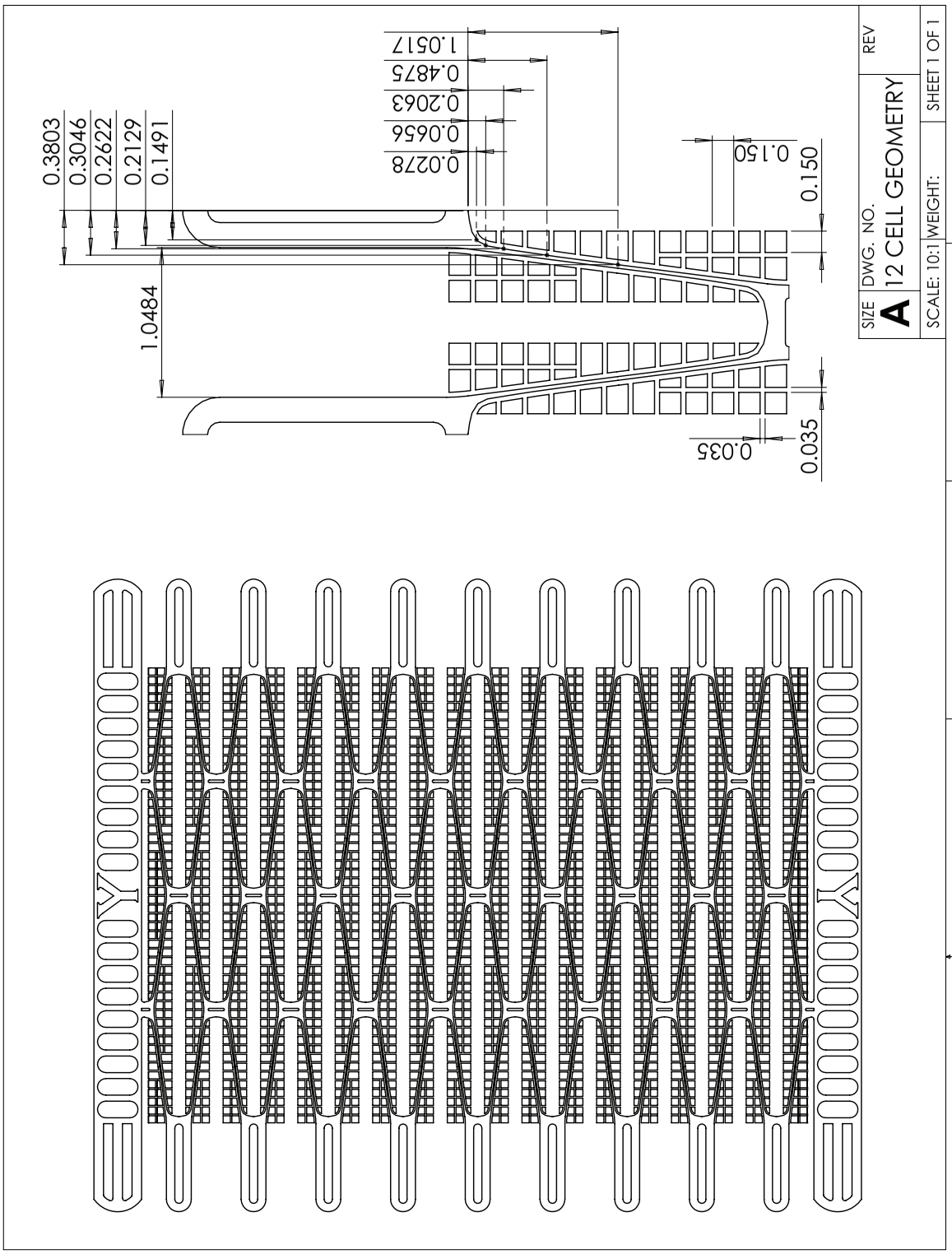

Figure C.2: Critical Planar Dimensions of 12 Cell Semi-Auxetic Design

C.2 10 Cell Cylindrical FEA Simulation Results

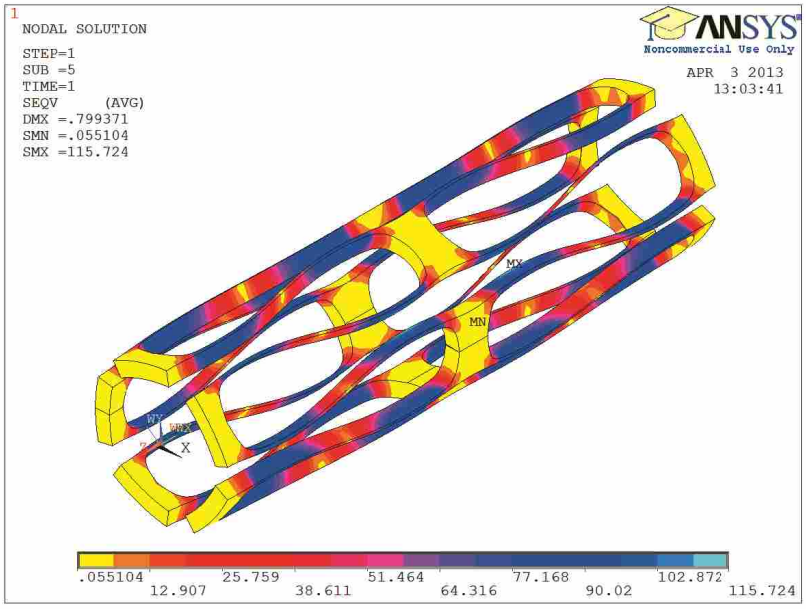

Figure C.3: ANSYS finite element model of 10 Cell design applied in a cylindrical configuration showing maximum stress values

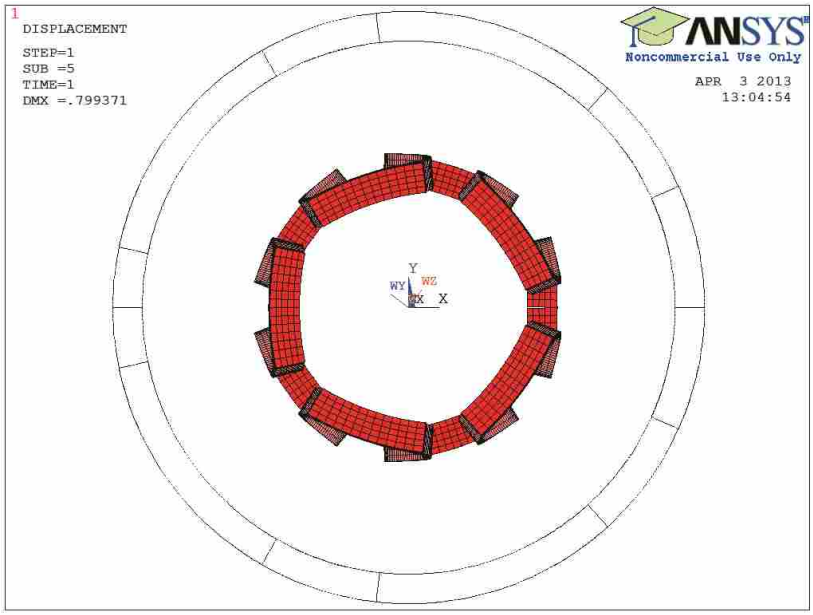

Figure C.4: ANSYS finite element model of 10 Cell design applied in a cylindrical configuration showing 3mm to 1mm diameter compression

APPENDIX D. EXAMPLES OF CODE USED IN THESIS RESEARCH

D.1 ANSYS Code to Calculate Modulus and Simulate Compression/Expansion

```
!! This code calculates the modulus of elasticity
!! based on an input of force and displacement for
!! the given geometry.

! Note all dimensions/constants in mm from iges import

finish
/CLEAR,NOSTART

/Begin

*set,ex,20000 !Initial modulus (MPa)
*set,testforce,-.0466 !Test force input (N)
*set,thick,0.330 !Sample thickness (mm)
*set,disp,-6.5 ! !Sample displacement (mm)

!Beginning of iterative loop
check = 1
numloop = 0
*DOWHILE,check

!Code to import IGS geometry
/AUX15
/CWD,'J:\'
IOPTN,IGES,NODEFEAT
IOPTN,MERGE,YES
IOPTN,SOLID,no
IOPTN,SMALL,YES
IOPTN,GTOLER, DEFA
IGESIN,'finalplanar_v2','IGS','groups\cmrvault\To Be Sorted\Compliant
 Mechanisms\MEMS\Kristopher Jones\grad\final design\geometry\'
LPLOT
/CWD,'C:\TEMP'
```

```
FINISH

/PREP7

LESIZE,ALL,.03, , , ,1, , ,1,   !element line size

ET,1,PLANE183   !element type

KEYOPT,1,1,0
KEYOPT,1,3,3
KEYOPT,1,6,0
KEYOPT,1,10,0

R,1,thick,  !calls thickness of material

!material properties (modulus and poisson's ratio)
MPTEMP,1,0
MPDATA,EX,1,,ex
MPDATA,PRXY,1,,.27

!Separates geometry into central target area
wpoffs,,1.884957
wprota,,90
asbw,all
wprota,,-90
wpoffs,,9.42477
wprota,,90
asbw,all
wprota,,-90
wpoffs,,-1.884957-9.42477
allsel,all

!mesh the geometry
numcmp,all
mshape,0,2d
mshkey,2
amesh,all

finish

/sol

!boudary conditions
dl,92,,ux,0
dl,92,,uy,disp
```

```
dl,92,,uz,0

dl,98,,ux,0
dl,98,,uy,disp
dl,98,,uz,0

dl,160,,ux,0
dl,160,,uy,0
dl,160,,uz,0

dl,166,,ux,0
dl,166,,uy,0
dl,166,,uz,0

FINISH

/SOL
!define analysis type, steps, and output
ANTYPE,0
NLGEOM,1
NSUBST,40,45,35
OUTRES,ERASE
OUTRES,all,ALL

/aux15 !set working directory to solve
/CWD,'C:\TEMP'
/solu
SOLVE

finish
/post1

!pull the reaction force in the y direction
PRRSOL,FY
FSUM,,
*GET,ANSYSforce,FSUM,0,ITEM,FY
allsel,all

!peform check and adjust modulus linearly
check = (testforce-ANSYSforce)**2
Eratio = testforce/ANSYSforce
ex = ex*Eratio
*IF,Eratio,eq,1.0000,EXIT

!pull displacement of target area
```

```
allsel,all
*get,lower,node,978,u,y
allsel,all
*get,upper,node,10140,u,y
allsel,all

*set,TA_disp,upper-lower

!clear geometry and load steps for next iteration
/SOL
LSCLEAR,ALL
/PREP7
aclear,all
adele,all,,,1
kdele,all
mpdele,prxy,1
mpdele,ex,1
etdele,all

numloop = numloop+1
*ENDDO
```

D.2 ANSYS Code to Model Semi-Auxetic Planar Stent Geometry Applied in a Tubular Configuration

```
!!This ANSYS code builds the cylindrical geometry
!!of the ci-cnt stent and compresses it radially

! Note all dimensions/constants in mm from iges import

finish
/CLEAR,NOSTART
/Begin

!Import surface to build geometry
/AUX15
/CWD,'J:\'
IOPTN,IGES,NODEFEAT
IOPTN,MERGE,YES
IOPTN,SOLID,no
IOPTN,SMALL,YES
```

```
IOPTN,GTOLER, DEFA
IGESIN,'tubular10','IGS','J:\groups\cmrvault\To Be Sorted\
 Compliant Mechanisms\MEMS\Kristopher Jones\Grad\Final Design\geometry\'
LPLOT
/CWD,'C:\TEMP'
FINISH

!Choose working directory
/CWD,'C:\TEMP'

FINISH
/PREP7

!Choose coordinate system and element types
CSYS,1
et,1,shell281
et,2,solid95

!Rotate WP for modeling
wprota,,,90
wprota,,90
wprota,,-72
asbw,all
wprota,,-72
asbw,all

!Choose element line size
LESIZE,ALL,.05, , , ,1, , ,1,

!mesh the surface
numcmp,all
mshape,0,2d
mshkey,2
type,1
amesh,all

!choose extrusion options
allsel,all
type,2
extopt,esize,5
extopt,aclear,1

!extrude surface radially
VEXT,all, , ,-.075,0,,,,,
csys,0
```

```
!reflect volume accross plane
VSYMM,Y,all, , , ,0,0
csys,1

KEYOPT,2,1,0
KEYOPT,2,5,0
KEYOPT,2,6,0
KEYOPT,2,11,0

!material properties
MPTEMP,,,,,,,,
MPTEMP,1,0
MPDATA,EX,1,,27000
MPDATA,PRXY,1,,.27
numcmp,all
allsel,all

!select lines for boundary conditions
LSEL,s, , ,3
LSEL,a, , ,323
LSEL,a, , ,236
LSEL,a, , ,31
LSEL,a, , ,11
LSEL,a, , ,246

!select nodes attached to lines
NSEL,ALL
NSLL,S,1
NPLOT

!nodal boundary conditions
nrotat,all
d,all,ux,-.75
d,all,uy,0
d,all,uz,0

allsel,all

!select areas for boundary conditions
asel,s,,,36
asel,a,,,117
asel,a,,,48
asel,a,,,129
```

```
NSLa,S,1
NPLOT

!surface rotation boundary conditions
nrotat,all
d,all,uy,0

allsel,all

FINISH
/SOL

!set nonlinear analysis, steps, and output
ANTYPE,0
NLGEOM,1
NSUBST,20,15,25
OUTRES,ERASE
OUTRES,ALL,ALL

!reset working directory
/aux15
/CWD,'C:\TEMP'


/solu
SOLVE
```

D.3 MATLAB Code for Data Processing

```
% This m file takes the raw data from the data_import.m file
% of compression testing and performs typical data processing
% such as unit conversion, normalization, zero-offset asjustment
% and plots the data.
clc;
clear;
clf;

% Change default text fonts.
set(0,'DefaultTextFontname', 'Times New Roman')
set(0,'DefaultTextFontSize', 11)
```

```
%Load the Raw Data
load('rawdata.mat')

%Adjust Test 11 (ID2A) Darrel design for having only 5 "springs"
mat(:,2,11) = mat(:,2,11).*1.2;

%Convert all force data to Newtons
mat(:,2,:) = mat(:,2,:).*9.81;

%Thickness Values for each sample (mm)
thick = [.3683 .4318 .254 .5588 .381 .2794 .254 .5842 .5207 .2032 ...
         .5461 .5080 .5207 .2159 .5969];

%Flexible length for each sample(mm)
flex_l = [1 14.1372 10.0440 15.0796 15.0796 10.0440 14.1372 10.0440 10.0440...
          15.0796 10.0440 10.0440 10.0440 14.1372 14.1372];

%Width of each sample (mm)
width = [1 9.6 13.279 10.6 10.6 13.279 9.6 13.279 13.279 10.6...
         13.279 13.279 13.279 9.6 9.6];

%Offset of zero displacement values (mm)
disp_adj = [.0001 .1595 .2652 .3948 .1095 .1892 .2845 .2706 .19 .4947 ...
            .3794 .685 .2953 .375 .195];

%Location (displacement) of break/buckle (mm)
br_buck = [0 4.6 3.65 4.245 4.69 3.111 4.2 3.83 2.07 4.889...
           4.395 5.025 1.624 4.375 2.474];

%Location (displacement) of End of Test (mm)
eot = [0 6 4.15 8.8 6.671 3.486 6.22 5.7 4.455 7.022 ...
       6.165 5.38 6.883 7.734 8.04];

%This loop goes through each set of data and performs
%processing on each one
for j=1:23

    %filter out noise
    mat(:,2,j) = smooth(mat(:,2,j),7);

    %locate zero starting point of
    ind = find(mat(:,1,j)<=(-1)*disp_adj(j),1);

    %create dummy matrix for processing
    mat2 = mat(:,:,j);
```

```
    %remove offset of displacement data and adjust
    %force data accordingly on dummy matrix
    mat2(1:length(mat2)-ind+1,:)=mat2(ind:end,:);
    mat2(:,1) = mat2(:,1)-mat2(1,1);
    spind=mat2(1:100,:);
    mat2(find(mat2>=0))=0;
    mat2(find(mat(:,:,j)==0))=nan;
    mat2(1:100,:)=spind;

    %replace data with processed data from dummy matrix
    mat(:,:,j)=mat2;

    %% First buckle/break
    %create data matrices of the processed data only up to
    %the first buckle/break
    fb_b_mat = mat;
    ind2 = find(mat(:,1,j)<=(-1)*br_buck(j),1);
    fb_b_mat(ind2:end,:,j) = nan;
    maxes(j,:) = -1*[ min(fb_b_mat(:,1,j)) min(fb_b_mat(:,2,j))]

    %% End of Test Adjustment
    %adjust ending of data and remove data after final fracture
    eot_mat = mat;
    ind3 = find(mat(:,1,j)<=(-1)*eot(j),1);
    mat(ind3:end,:,j) = nan;
    max_disp(j) = min(mat(:,1,j));


end

%transpose and output max displacement
max_disp = max_disp'

% set up colors for plots
x = [.5 0 .5;1 0 1;1 0 .5;0 1 0;.75 .75 .75;.5 .5 .5;0 0 0;1 0 0;0 .45 0];

%%

% Normalize data based on thickness and flex length
for i=1:23
    mat_norm(:,2,i) = mat(:,2,i)./(thick(i));
    mat_norm(:,1,i) = mat(:,1,i)./flex_l(i);
end
```

```
%% Plots for 10 Cell data

j = [4 5 10 20 21 22 23];

%As tested data plot
for i=j
   figure(2)
   plot(-1.*mat(:,1,i),-1.*mat(:,2,i),'Color',x(find(j==i),:),...
'LineWidth',2)
   hold on
end
hold off
grid on
legend('T4ID11','T5ID15','T10ID23',...
       'T20ID13A','T21ID17A','T22ID20A','T23ID21A','Location',...
'NorthEastOutside')
title('"10 Cell" Design')
xlabel('Deflection (mm)')
ylabel('Force (N/mm)')

j = [4 5 10 20 21 22 23];

%Normalized data plot
for i=j
   figure(5)
   plot(-1.*mat(:,1,i),-1.*mat_norm(:,2,i),'Color',x(find(j==i),:),...
'LineWidth',2)
   hold on
end
hold off
grid on
legend('T4ID11','T5ID15','T10ID23',...
       'T20ID13A','T21ID17A','T22ID20A','T23ID21A','Location',...
'NorthEastOutside')
title('"10 Cell" Design')
xlabel('Deflection (mm)')
ylabel('Normalized Force (N/mm)')

%% Plots for 12 Cell data

j = [2 7 14 15 16 17 18 19];

% As tested data plot
for i=j
   figure(3)
```

```
   plot(-1.*mat(:,1,i),-1.*mat(:,2,i),'Color',x(find(j==i),:),...
'LineWidth',2)
   hold on
end

grid on
legend('T2ID7','T7ID20',...
       'T14ID5A','T15ID6A','T16ID7A','T17ID8A','T18ID9A',...
'T19ID10A','Location','NorthEastOutside')
title('"12 Cell" Design')
xlabel('Deflection (mm)')
ylabel('Force (N)')

j = [2 7 14 15 16 17 18 19];

%Normalized data plot
for i=j
   figure(6)
   plot(-1.*mat(:,1,i),-1.*mat_norm(:,2,i),'Color',...
x(find(j==i),:),'LineWidth',2)
   hold on
end

grid on
legend('T2ID7','T7ID20',...
       'T14ID5A','T15ID6A','T16ID7A','T17ID8A','T18ID9A',...
'T19ID10A','Location','NorthEastOutside')
title('"12 Cell" Design')
xlabel('Deflection (mm)')
ylabel('Normalized Force (N/mm)')
```

D.4 ANSYS Code for Optimization of Spline

```
!!This code creates geometry and sets material
!!properties up for the optimization of a
!!spline curve

finish
/clear,start
/Begin
```

```
!set constants
pi = 3.1415926535
*set,cell_n,12
*set,disp,-.5 (mm)
*set,mfw,.025 !minimum flex width (mm)
*set,hcw,2.25 !half cell width (mm)

!set up dependant variables' equations
*set,rw,.15
*set,rh,pi/((cell_n/2)+.5)
*set,theta,atan(((3*pi-cell_n*rh)/cell_n)/hcw)
*set,delx,(hcw/2-rw/2)/5
*set,min_slope,(rh/2+((3*pi-cell_n*rh)/(2*cell_n))
-cos(theta)*mfw/2)/(hcw/2+rw/2+sin(theta)*mfw/2)

!out of plane thickness (mm)
*set,thick,0.200

!define large and small element sizes
*set,elarge,.05
*set,esmall,.0075

!define modulus (MPa)
*set,ex,10000

!define "y" location of spline points (doubles as upper limit)
*set,k10,(((3*pi-(cell_n)*rh)/(cell_n*hcw))*(rw/2+hcw/16)+
 (rh/2)-(rw/2)*tan(theta)-mfw/(2*cos(theta)))

!define "y" location of spline points (doubles as upper limit)
*set,k11,((3*pi-(cell_n)*rh)/(cell_n*hcw))*(rw/2+hcw/8)+
 (rh/2)-(rw/2)*tan(theta)-mfw/(2*cos(theta))

!define "y" location of spline points (doubles as upper limit)
*set,k12,((3*pi-(cell_n)*rh)/(cell_n*hcw))*(rw/2+hcw/4)+
 (rh/2)-(rw/2)*tan(theta)-mfw/(2*cos(theta))

/PREP7
!set up parametric keypoints
K,1,0,0,0,
k,2,rw,0,0
k,3,0,rh/2+rw/2*tan(theta)
k,4,hcw,2*rh/2+((3*pi-cell_n*rh)/cell_n)
k,5,hcw+rw,2*rh/2+((3*pi-cell_n*rh)/cell_n)
k,6,hcw+rw,2*rh/2+((3*pi-cell_n*rh)/cell_n)-(rh/2+
```

```
 rw/2*tan(theta))
k,7,hcw/2+rw/2,rh/2+((3*pi-cell_n*rh)/(2*cell_n))
k,8,hcw/2+rw/2+sin(theta)*mfw/2,rh/2+
 ((3*pi-cell_n*rh)/(2*cell_n))-cos(theta)*mfw/2
k,9,hcw/2+rw/2-sin(theta)*mfw/2,rh/2+
 ((3*pi-cell_n*rh)/(2*cell_n))+cos(theta)*mfw/2

!connect keypoints with lines
lstr,1,2
lstr,1,3
lstr,3,9
lstr,4,5
lstr,5,6
lstr,6,8

!set optimizable keypoints locations
k,10,rw/2+hcw/16,k10
k,11,rw/2+hcw/8,k11
k,12,rw/2+hcw/4,k12

!create spline between appropriate points
BSPLIN,2,10,11,,,12,0,-1,0,cos(theta),sin(theta),0
l,12,8

!set opposite optimizable keypoints locations
k,15,hcw-hcw/4+rw/2,2*rh/2+((3*pi-cell_n*rh)/cell_n)-k12
k,16,hcw-hcw/8+rw/2,2*rh/2+((3*pi-cell_n*rh)/cell_n)-k11
k,17,hcw-hcw/16+rw/2,2*rh/2+((3*pi-cell_n*rh)/cell_n)-k10

!create opposite spline between appropriate points
bsplin,15,16,17,,,4,-cos(theta),-sin(theta),0,0,1,0
l,9,15

!create area and apply material/geometry properties
al,all
ET,1,PLANE183
KEYOPT,1,1,0
KEYOPT,1,3,3
KEYOPT,1,6,0
KEYOPT,1,10,0
R,1,thick,
MPTEMP,1,0
MPDATA,EX,1,,ex
MPDATA,PRXY,1,,.27
numcmp,all
```

```
!separate the area into different
!regions for meshing (large and small)
wpave,,(rh/2+rw/2*tan(theta))
wprota,,-90
wprota,,,30
asbw,all
wprota,,,-30
wprota,,90
wpave,,-(rh/2+rw/2*tan(theta))

wpave,hcw+rw,2*rh/2+((3*pi-cell_n*rh)/cell_n)-(rh/2+
 rw/2*tan(theta))
wprota,,-90
wprota,,,30
asbw,all
wprota,,,-30
wprota,,90
wpave,-(hcw+rw,2*rh/2+((3*pi-cell_n*rh)/cell_n)-(rh/2+
 rw/2*tan(theta)))

!mesh areas
numcmp,all
mshape,1,2d
mshkey,0
ESIZE,esmall,
amesh,3
mshape,0,2d
mshkey,1
esize,elarge
asel,s,,,1,2
amesh,all
allsel,all

!boundary conditions
DL,4, ,UY,disp   !mm
DL,1, ,UY,0
DL,1, ,UX,0

!apply nonlinear analysis
ANTYPE,0
NLGEOM,1

!set working directory
/aux15
```

```
/CWD,'C:\TEMP'
/solu
SOLVE

!obtain maximum stress data for optimization
/post1
PLNSOL, S,EQV, 0,1.0
*get,maxstress,PLNSOL,,max

!!This portion of the code is a separate file

/opt
!select batch optimization driver batch file
OPANL,'curve2','txt','J:\Grad\Stent CAD\Curve Analysis\curve2.txt

!upper and lower bounds for variables and variable resolution
OPVAR,K10,DV,(min_slope)*(rw/2+hcw/16),(((3*pi-(cell_n)*rh)/(cell_n*hcw))
*(rw/2+hcw/16)+(rh/2)-(rw/2)*tan(theta)-mfw/(2*cos(theta))),.005,
OPVAR,K11,DV,(min_slope)*(rw/2+hcw/8),(((3*pi-(cell_n)*rh)/(cell_n*hcw))
*(rw/2+hcw/8)+(rh/2)-(rw/2)*tan(theta)-mfw/(2*cos(theta))),.005,
OPVAR,K12,DV,(min_slope)*(rw+3*delx/2),((3*pi-(cell_n)*rh)/(cell_n*hcw))
*(rw+3*delx/2)+(rh/2)-(rw/2)*tan(theta)-mfw/(2*cos(theta)),.005,

!choose variable to minimize
OPVAR,maxstress,OBJ, , ,.03,

!optimization settings
OPTYPE,FIRS
OPFRST,20,100,.2,
```